Wave propagation modelling approach for improved assessment of the acoustic field in closed test section wind tunnels

Mourão Bento, Hugo F.; VanDercreek, Colin P.; Avallone, Francesco; Ragni, Daniele; Sijtsma, Pieter; Snellen, Mirjam

Citation (APA)

Important note
To cite this publication, please use the final published version (if applicable).
Please check the document version above.

Wave propagation modelling approach for improved assessment of the acoustic field in closed test section wind tunnels

Hugo F. Mourão Bento [a],*, Colin P. VanDercreek [a], Francesco Avallone [b], Daniele Ragni [a], Pieter Sijtsma [a], Mirjam Snellen [a]

[a] *Faculty of Aerospace, Delft University of Technology, Delft 2629HS, The Netherlands*
[b] *Politecnico di Torino, Corso Duca degli Abruzzi 24, Torino 10129, Italy*

ARTICLE INFO

ABSTRACT

Sound propagation in closed test section wind tunnels suffers from reflections and diffraction, which compromise acoustic measurements. In this article, it is proved possible to improve the post-processing of phased-array microphone measurements by using an approach based on the combination of numerical acoustic simulations and beamforming. A Finite Element Method solver for the Helmholtz equation is used to model the acoustic response of the experimental facility. The simulations are compared with acoustic experiments performed at TU Delft's Low Turbulence Tunnel, using both fully reflective (baseline) and lined test sections. The solver accurately predicts the acoustic propagation from a monopole sound source at the centre of the test section to the microphones in the phased-array, for frequencies in the range $500\,\text{Hz} < f < 2000\,\text{Hz}$. It is shown that a (lower fidelity) geometric modelling method is unable to precisely predict the acoustic response of the Low Turbulence Tunnel at these frequencies, due to strong acoustic diffraction. The numerical results are used to implement corrections to the post-processing of experimental data. A corrected version of the Source Power Integration method is able to increase the accuracy of the source's noise levels calculation, based on a single numerical simulation with the source at the same location as in the experiment. A Green's function correction increases the beamforming resolution and the source's noise levels estimation accuracy from the beamforming maps, without a priori knowledge of the source's location. Both corrections perform well at processing flow-on acoustic measurements, and the Green's function correction shows an additional benefit. The improvement in beamforming spatial resolution leads to an increase of the signal to noise ratio.

1. Introduction

Wind tunnels with a closed test section provide a higher aerodynamic fidelity than their open-jet counterparts. In open-jet test sections, flow can be disturbed by jet deflection, or by the interaction between the jet and the collector [1]. However, along with the increased aerodynamic background noise [2], strong reflections in a closed test section decrease the reliability of acoustic measurements [3,4]. Mitigation strategies to reduce the detrimental effects of reflections (e.g., acoustic interference) include lining the tunnel walls with sound absorbing materials [5,6], and making use of post-processing methods to identify the primary aerodynamic noise source of interest [7].

Acoustic beamforming techniques, using phased-microphone arrays, enable the quantification of noise from distinct sources [8]. Beamforming also improves the signal-to-noise ratio, e.g., with respect to aerodynamic background noise, in comparison with results obtained from single microphone measurements [9]. When the beamforming spatial resolution is sufficiently high to separate the distance between a source and its reflections, this signal processing technique is able to reduce the adverse impact of reflections on acoustic measurements. However, the limited resolution of the different beamforming methods complicates the task of distinguishing sound sources. The resolution of conventional beamforming algorithms is particularly poor at frequencies near and below the Rayleigh limit [10].

Typically, conventional beamforming takes into account the sound propagation (through the Green's function) from a source to an observer by assuming the source to behave as a free-field monopole. Previous literature has been directed at reducing the effect of non-free-field conditions, e.g. reflections in the setup, on beamforming results. Guidati et al. [11] and Fenech and Takeda [12] used a geometric modelling algorithm to predict and correct for the influence of mirror-reflections on the propagation of sound in a rectangular wind tunnel test section. Sijtsma and Holthusen [13] reduced the influence of specular reflections in the beamforming map with a "Mirror Minimisation" technique, a correction which is less dependent on the assumed strength and location of the mirror sources. Fischer and Doolan [14] improved beamforming in a closed hard-walled wind tunnel by calculating corrected Green's functions based on the mirror-source method and on experimental measurements. The Green's function obtained experimentally achieved better results, however, it requires a complex measurement procedure. The experimental Green's function had to be measured for each beamforming scan grid location. Gombots et al. [15] used a Finite Element Method (FEM) for estimating the Green's function of sound propagation in a disturbed environment, which has been shown to be accurate for identifying and quantifying sources simulated numerically. Lehmann et al. [16] also employed a numerical method, the Boundary Element Method, for calculating the acoustic Green's function in a disturbed environment. The numerical Green's function has been shown to improve the beamforming maps of experimental data, measured with a setup representative of a fan in a heat exchanger, e.g., by reducing the main lobe width.

Preceding literature has, however, not yet been able to demonstrate that a numerically obtained Green's function correction improves the estimation of an experimental source's noise levels. In this study, simulations of an acoustic source inside a wind tunnel test section were done with a FEM solver for the Helmholtz equation. The numerical results are validated with an acoustic experiment carried out at TU Delft's Low Turbulence Tunnel (LTT), which has been adapted for aeroacoustics studies, e.g., [17,18]. Following, two methods are proposed for correcting the acoustic experimental results, making use of the FEM simulations. In the first method, the Green's function is corrected, similarly to the approach employed in literature, e.g., [15,16]. In the second method, only the Source Power Integration (SPI) step is modified, making use of prior knowledge of the source location. SPI is a technique commonly used to estimate source noise levels from beamforming maps [19]. The second method removes the need of having to compute the Green's function in the entire test section, or at the beamforming scan plane. To quantify the benefits achieved with each correcting method, an experimental measurement of the source in an undisturbed environment is used as reference. To the authors' knowledge, this is the first time that the approach of lining a closed wind tunnel test section is combined with the approach of numerically simulating the wind tunnel's acoustic response, for improving the experimental beamforming results.

The study is structured as follows. Section 2 describes the methodology employed in the study, including the computational approach, the experimental campaign, and the post-processing methods. Section 3 covers the validation and verification of the results presented. Section 4 describes the dominant acoustic phenomena present in the wind tunnel test section, based on the computational solutions. Section 5 presents the results obtained after implementing the numerically obtained corrections for processing the experimental data with beamforming. The discussion of the applicability of the post-processing methodology proposed in this paper to flow-on measurements is presented in Section 6. Finally, Section 7 highlights the main conclusions from the study.

2. Methodology

2.1. Numerical modelling of sound wave propagation

The FEM solver *COMSOL Multiphysics* was used to solve the wave equation:

$$\frac{1}{c^2}\frac{\partial^2 p}{\partial t^2} - \nabla^2 p = 0, \tag{1}$$

where c is the sound speed, p is pressure, t is time, and ∇ is the nabla operator. The *Pressure Acoustics Frequency Domain interface*, part of the *Acoustics module*, was used. The iterative solver assumes the acoustic source terms and consequent pressure fluctuations to be time-harmonic, to reduce Eq. (1) to the Helmholtz equation:

$$\nabla^2 p + \frac{\omega^2}{c^2} p = 0, \tag{2}$$

where ω is the angular frequency. In this study, an acoustic monopole source was introduced in the simulations by adding a sphere whose surface was defined by the normal acceleration boundary condition:

$$\boldsymbol{n} \cdot \nabla p = \rho a_n, \tag{3}$$

where $\boldsymbol{n}$ is the wall normal vector and a_n is the inward normal acceleration. Both the speed of sound and the fluid density, ρ, were assumed constant. These were calculated based on the ambient pressure, 1 atm, and ambient temperature, 15 °C, making use of the ideal gas assumption. The sound hard boundary and the symmetry boundary conditions were included in the simulation by imposing Eq. (3) with $a_n = 0$ at these boundaries [20].
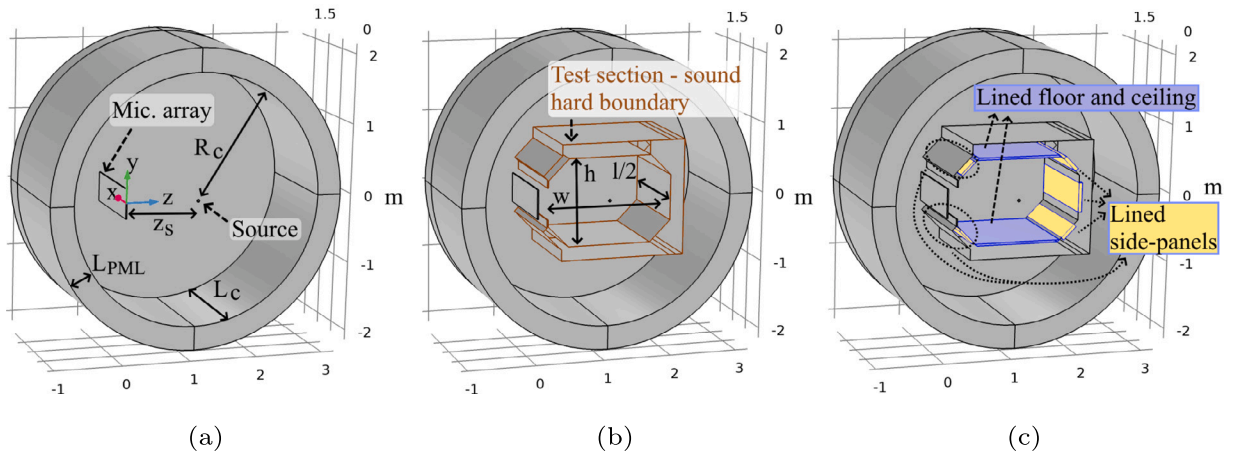
Fig. 1. Numerical setup used for the Finite Element Method acoustic simulations: setup defined for the simulation of a free-field monopole (a); setup of the baseline wind tunnel test section (b); and setup of the fully lined test section configuration (c).

The porous Melamine lined wind tunnel walls were modelled by defining an equivalent fluid domain, at the location of the lining [20]. In these porous fluid regions, pressure waves are dissipated according to the Delany–Bazley–Miki model [21]. This empirical model allows for the prediction of sound absorption in a porous liner with a porosity close to 1, as is the case of Melamine foam, based on the material's viscous resistivity [22]. The porous materials are the only regions inside the test section where acoustic dissipation occurs, as thermoviscous effects were neglected outside of the porous domains. Atmospheric dissipation was considered negligible, due to the relatively small size of the numerical domain. Furthermore, the simulations were conducted for flow-off scenarios, in which no viscous losses associated with wall boundary layers occur. Reflections at the boundary of the simulation domain were avoided by defining Perfectly Matched Layer (PML) regions, where outgoing waves are dampened. As in [9], this approach allowed for the simulation of an acoustically open domain [20]. This study evaluates each setup for the acoustic frequencies in the range $300\,\text{Hz} \leq f \leq 2000\,\text{Hz}$, with steps of $\Delta f = 10\,\text{Hz}$.

2.1.1. Numerical setup

Fig. 1 shows the numerical setups defined for understanding the acoustic behaviour of the different wind tunnel test section (TS) configurations. Fig. 1(a) shows the setup defined for the reference simulation, the simulation of a free-field monopole source. The acoustic domain has a cylindrical shape, with streamwise (x–direction) length $L_c = 1.65\,\text{m}$ and radius $R_c = 1.8\,\text{m}$. Outside the acoustic domain, the PML regions were placed. The thickness of the PML regions depend on the acoustic wavelength, λ, of each simulation: $L_{\text{PML}} = 2\lambda$. The monopole source is a sphere of radius $0.02\,\text{m}$, placed at the centre of the cylindrical domain, with coordinates $(x_s, y_s, z_s) = (0, 0, 1.05)\text{m}$. Only half of the sphere is simulated, as a symmetry boundary condition is placed at the streamwise plane that passes through the centre of the source. This plane is defined by $x = 0$. The microphone array used to measure the source's noise levels in the simulation is placed at $z = 0$ and is confined within $-0.4\,\text{m} < y < 0.4\,\text{m}$ and $x < 0.8\,\text{m}$.

The vertical and spanwise coordinates of the 62 microphones that make up the array are the same as in the wind tunnel experiment (described with more detail in Section 2.3). The streamwise coordinates of the simulated array are $x_{\text{simulation}} = |x_{\text{experiment}}|$, where $|\cdot|$ is the modulus, so that all microphones have a positive streamwise coordinate, and are thus placed inside the simulation domain. A rectangular box is seen in Fig. 1(a) which encloses the microphone array. The box has been exclusively defined for increasing cell refinement at the measurement location.

Fig. 1(b) shows the simulation setup of the baseline wind tunnel test section. The test section has an octagonal shape with a constant angle between walls of 135°. The test section's height, spanwise width and streamwise (half) length are $h_{\text{TS}} = 1.25\,\text{m}$, $w_{\text{TS}} = 1.8\,\text{m}$ and $l_{\text{TS}}/2 = 1.4\,\text{m}$. l_{TS} is larger in the simulation than in the experiment to allow for the assumption that the simulated test section is infinite in the streamwise direction, from the perspective of the microphone array (see description of the post-processing technique in Section 2.4.2). Fig. 1(c) shows the setup of the fully lined test section configuration. The floor and ceiling are lined with $3\,\text{cm}$ thick melamine panels, simply placed over the baseline floor and ceiling (seen in Fig. 1(b)). The side panels are lined with $5\,\text{cm}$ thick melamine, installed in panels which are mounted on the walls, effectively increasing the fluid volume inside the test section. The melamine side panels are enclosed (on 5 sides) by walls, where the sound hard wall boundary condition is imposed. Sound reflections still occur at these walls, mainly at lower frequencies. The sound absorption characteristics of Melamine foam panels with $3\,\text{cm}$ and $5\,\text{cm}$ thickness placed over a solid wall are dictated by Melamine's viscous resistivity, $R_v = 9\,\text{kPa s m}^{-2}$, and are detailed in Ref. [23].

Table 1 describes the different setups evaluated in this study. The Reference, Test section A and Test section D simulation domains are shown, respectively, in Figs. 1(a)–1(c). B and C are configurations with intermediate lining, between the baseline (A) and the fully lined (D) cases. Besides simulating the complete test sections, the dominance of specular reflections and diffraction was also evaluated by performing simulations with a reduced number of wind tunnel walls. This is done in order to isolate each of the

Table 1

Numerical setups designed for the FEM simulations of a monopole sound source.

Setup designation	Details	Bottom and top 3 cm melamine lining	Side-panels lined with 5 cm melamine
Reference	Free-field monopole	–	–
Test section A	Baseline section	–	–
Test section B	Lined section	✓	–
Test section C	Lined section	–	✓
Test section D	Fully lined TS	✓	✓
2 walls	Floor and opposite wall	–	–
3 walls	Floor, ceiling and opposite wall	–	–
Walls + corner(s)	Corner(s) between the floor/ ceiling and opposite wall	–	–
Walls + edge(s)	Being edges the angled walls between floor/ceiling and the array	–	–
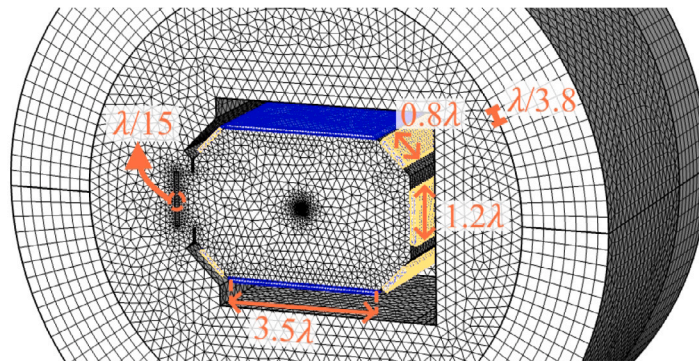
Fig. 2. Computational grid generated for the numerical simulation of test section D, the fully lined configuration. Element size correspondent to the simulation of the source emitting noise at $f = 1$ kHz, with the coarse grid settings. The elements coloured with blue represent the melamine lining regions over the floor and ceiling, and the elements coloured with yellow represent the lined side-panels. (For interpretation of the references to colour in this figure legend, the reader is referred to the web version of this article.)

dominant acoustic phenomena. For these simulations, the domain streamwise length and the walls' half streamwise length were reduced, respectively, to $L_c = 1.25$ m and $l/2 = 1$ m. The remaining setup geometrical characteristics and boundary conditions, as shown in Fig. 1, are uniform for all setups described in Table 1.

2.1.2. Discretisation

Fig. 2 shows the coarse computational grid generated for studying the response of the fully lined test section, with the source emitting noise at 1000 Hz. The figure shows that the grid is unstructured, except for the PML domains, where a swept grid was introduced. For each computed frequency, the size of the mesh elements was defined based on the sound wavelength, λ. For the medium grids, the cell size has been defined to be not larger than $\lambda/5$. Regions of increased refinement include the inner walls of the test section, the acoustic source and the porous media. The region where the microphones are located have cells smaller or equal to $\lambda/20$, in order to avoid complex interpolations (i.e. non-linear interpolations) between cell elements during post-processing. A grid refinement study was conducted to find the optimum grid refinement. For the coarse and fine grids, the cell length settings of the medium grid were divided by 0.75 and 1.5, respectively. The results of the grid dependence study are discussed in Section 3.1.

2.2. Geometric modelling

To understand the influence of specular reflections in the acoustic behaviour of the octagonal wind tunnel test section, a Geometric Modelling (GM) algorithm was developed. The algorithm is an extension of the GM described in Refs. [23,24]. This algorithm is based on the mirror-source method, and therefore considers reflections in the test section to be specular, neglecting the existence of diffuse reflections. Diffraction inside the test section is also neglected in the present geometric model. The mirror-source method assumes the walls of the test section to be infinite, and loses accuracy at lower frequencies, when the acoustic wavelength becomes comparable to the size of the wall [25]. The method provides a good initial prediction of acoustic reflections on a single wall, with dimensions similar to the test section walls considered in this study (i.e. of the same order of magnitude) [24].

The specular reflections on the three larger walls of the test section (floor, ceiling and wall opposite to the array) are modelled as a mirror-source, as shown in Fig. 3. Primary, secondary and tertiary reflections refer to waves which reflect over one, two or three walls on the path between the source and a microphone. As in the numerical (FEM) setup, the microphones in Fig. 3 are
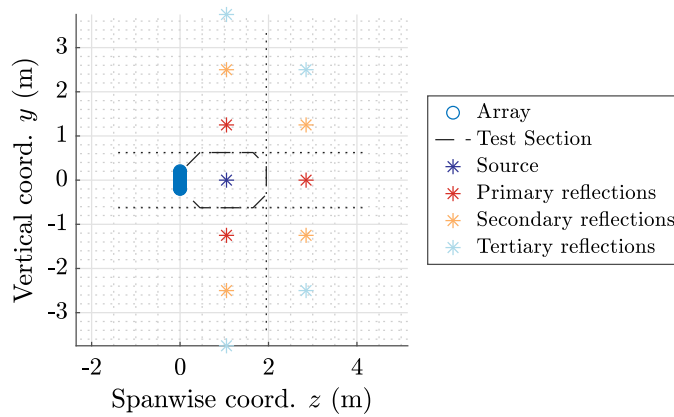
Fig. 3. Setup of the geometric modelling simulations. The reflections on the three largest test section walls (floor, ceiling and wall opposite to the array) are modelled with the mirror–source model.

located slightly (15 cm) outside the test section in the z direction. This is done in order to replicate the experimental installation of the microphone array. The experimental setup is detailed in the following sub-section.

The GM results provide clarity regarding the strength of mirror reflections in the test section. The comparison with FEM allows for the understanding of how the remaining acoustic phenomena, as diffraction or diffuse reflections, alter the test section's acoustic behaviour.

2.3. Experimental validation case

The wave propagation modelling method described in Section 2.1 has been validated against acoustic measurements taken at the Low Turbulence Tunnel (LTT), at TU Delft. The LTT is a closed wind tunnel circuit, initially designed for aerodynamic testing. The flow in the test section of 1.8 by 1.25 m can reach free-stream velocities, U_∞, up to $120\,\mathrm{m\,s^{-1}}$ [26]. For $U_\infty \leq 80\,\mathrm{m\,s^{-1}}$ the average turbulence intensity, Tu, remains below 0.05 % [27]. Due to the closed form of the LTT circuit, reflections throughout the wind tunnel contribute towards a long reverberation time [23], i.e., towards a slow decay of sound after an acoustic source has stopped emitting noise.

Acoustic reflections in the test section are dictated by its elongated octagonal shape, shown in Fig. 4(a). Figs. 4(b) and 4(c) show, respectively, the speaker installed in the baseline (fully reflective) test section and in the fully lined test section. The figures show that, for the experimental test section, the left side-panel is replaced by a Kevlar window, behind which the microphone array is placed.

The experimental data analysed in this study corresponds to measurements taken with the following free-stream velocities in the test section: $U_\infty = 0\,\mathrm{m\,s^{-1}}$, $U_\infty = 20\,\mathrm{m\,s^{-1}}$ and $U_\infty = 30\,\mathrm{m\,s^{-1}}$.

2.3.1. Aeroacoustic test section lining

The experimental campaign evaluates four different test section configurations (Table 2). The baseline (most reflective configuration) is shown in Fig. 4(b). The octagonal baseline test section contains 7 solid fully reflective walls. The Kevlar left side-panel is present in all four configurations, to allow measurements with the microphone array. The fully lined configuration (Figs. 4(a) and 4(c)) has the floor and ceiling lined with 3 cm Basotect melamine foam. This lining was attached to the baseline surfaces by gluing the foam to thin (few mm thick) wooden panels, which are connected to the test section walls with screws. On the 5 side-walls opposite and adjacent to the array, the baseline panels are substituted with lined panels. These lined side-panels consist of 5 cm thick wedged Basotect melamine, covered with a Kevlar sheet. Two intermediate test sections were also tested: one with the top and bottom flat melamine lining, and with the baseline side-panels, and the second with the baseline top and bottom, and with the lined side-panels. The main differences between the experimental and numerical test sections A to D (see Tables 1 and 2) are the presence of Kevlar in the experiment, which is not modelled numerically; and the experimental side-panels with wedged melamine lining, which is simplified to flat melamine in the numerical setup.

2.3.2. Reference acoustic source

The acoustic source seen in Fig. 4 is a miniature QindW speaker model, developed by QSources [28]. The speaker has omnidirectionality at low frequencies, up to 2 kHz [24]. Verification tests carried out at the TU Delft Anechoic wind tunnel (facility described in [29]) showed that the error in speaker omnidirectionality remains below ±2 dB, within the frequency range $300\,\mathrm{Hz} \leq f \leq 2000\,\mathrm{Hz}$. The speaker is placed at the centre of the test section, being aligned with the streamwise centre of the microphone array. The aerodynamic shape of the speaker results in low aerodynamic self-noise. For the flow-off tests, the speaker's input used a white-noise signal in the range 300 Hz to 6300 Hz.
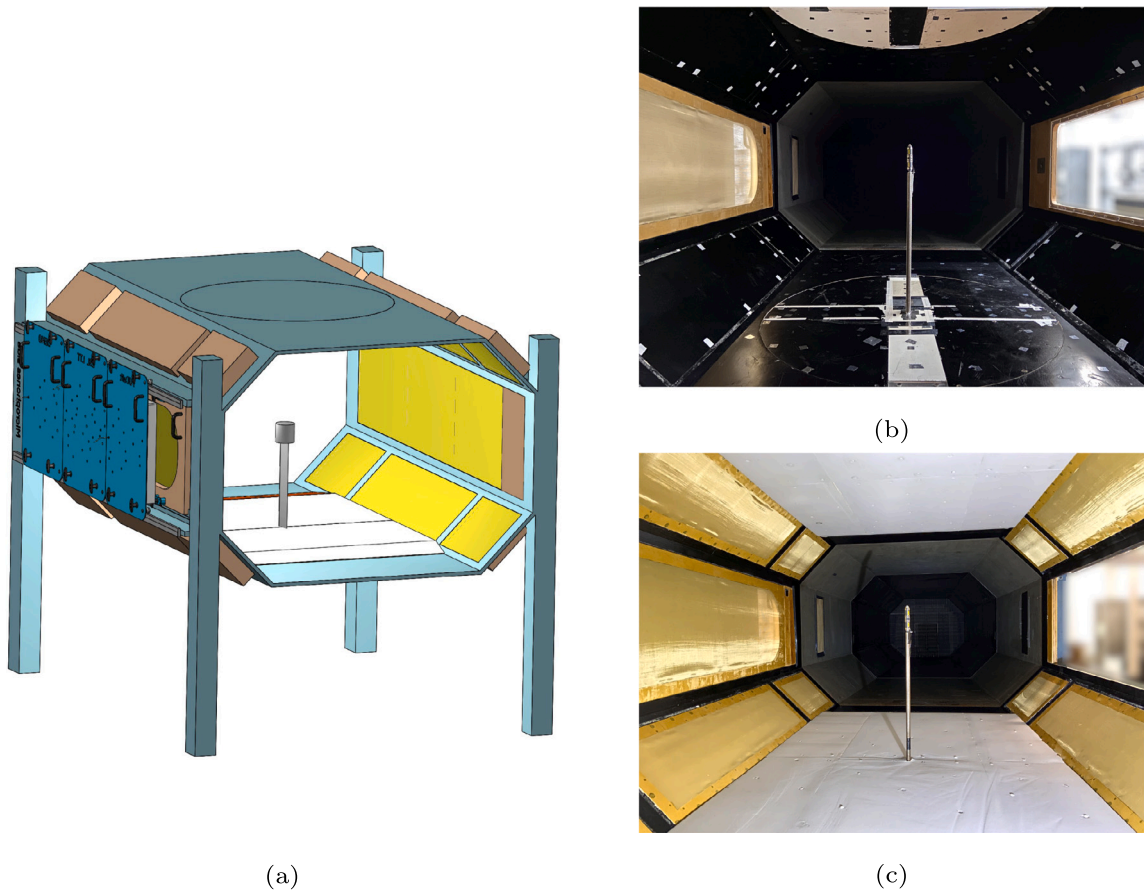
Fig. 4. Aeroacoustic test section of the Low Turbulence Tunnel, as seen from the inlet: computer-aided design rendering of the test section (a); test section with baseline reflective walls (b); and fully lined test section (c).

Table 2
Low Turbulence Tunnel test sections tested.

Test section	Microphone array recessed behind Kevlar	Top and bottom flat 3 cm melamine lining	Side-panels lined with 5 cm wedged melamine, covered by Kevlar
A, Baseline	✓	–	–
B, Intermediate	✓	✓	–
C, Intermediate	✓	–	✓
D, Fully lined	✓	✓	✓

For the flow-on tests, the signal provided to the speaker was based on a sum of sine waves, with constant amplitudes, at the frequencies of interest. This solution allows for the increase of the speaker's noise signature at each frequency, f. Two distinct signals were provided to the speaker: a sum of sinusoids in the range $f_1 = 325\,\text{Hz}$ to $f_{\text{end}} = 825\,\text{Hz}$ (low-frequency, narrow band), and a sum of sinusoids in the range $f_1 = 325\,\text{Hz}$ to $f_{\text{end}} = 2175\,\text{Hz}$ (broadband). The signals, $v(t)$, were calculated from:

$$v(t) = \sum_{f \in F} \sin(2\pi f t + \phi_{\text{rand}}), \tag{4}$$

where $F = \{f_1, f_1 + 5\,\text{Hz}, f_1 + 10\,\text{Hz}, \ldots, f_{\text{end}}\}$, ϕ_{rand} is a random phase shift applied to each sinusoid, and t is the time coordinate.

2.3.3. Acoustic measurement technique

The acoustic measurements were taken with a phased microphone array. The array consists of 62 PUI AUDIO 665–POM–2735P–R microphones. The array has an elliptical shape, extending 1.6 m in the streamwise direction and 0.4 m in the vertical direction, and is shown in Fig. 5(a). The microphones are held by a solid plate, lined with 5 cm plane melamine foam. The microphones are positioned flush with the foam surface. During measurements, the microphones are recessed 15 cm behind a stretched Aviation-standard Kevlar 49 T 965 sheet (see Figs. 4 and 5(b)). The main difference between the experimental and the numerical (see
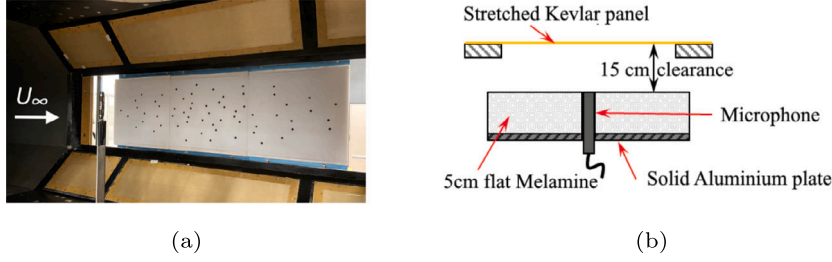
Fig. 5. Low Turbulence Tunnel microphone array: array installed in test section C, without the array's Kevlar panel (a); and microphone placement, behind the Kevlar panel (b). Figure (b) has been adapted from [30].

Section 2.1.1) microphone array setups is that the simulated microphones are placed as free-field microphones, i.e., without the lined plate holder and without the Kevlar sheet. The lined holder can cause an offset in the measured absolute noise levels at low frequencies, but this offset is negligible when evaluating the difference between the noise spectra of two test cases, e.g. the difference between the reference simulation and the simulation with a test section. The influence of the Kevlar panel on the measurements was verified by performing an additional measurement of the speaker noise with test section C without the Kevlar panel, i.e., with an open wall. This was possible since this measurement was taken with 0 free-stream velocity.

The microphones were calibrated with a Brüel & Kjaer 4230 pistonphone, at the frequency of $1\,\text{kHz}$. Each experimental acoustic measurement was taken with a measurement time of $20\,\text{s}$ and a sampling frequency of $50\,\text{kHz}$.

2.4. Post-processing algorithms

The numerical microphone data was extracted for each frequency, as the simulations were done with the frequency domain formulation. The experimental microphone data was instead measured in the time domain. The experimental microphone signals were converted to the frequency domain with the Welch's method [31]. The $20\,\text{s}$ signals were divided into windows of $0.1\,\text{s}$, with a $50\,\%$ overlap. Each window was multiplied by the Hanning function. The following steps in the post-processing were equally applied to both the experimental and the numerical microphone data, in the frequency domain.

Acoustic interference in the test section was quantified as the difference between the measurements in the reverberant environment and the reference speaker measurement, which was taken outside the wind tunnel test section, in a large room (with low reverberation) and with the microphone array described in Section 2.3.3. ΔSPL is defined as:

$$\Delta\text{SPL} = \text{SPL}_{\text{Speaker inside the test section}} - \text{SPL}_{\text{Reference, speaker}}, \tag{5}$$

being Sound Pressure Level defined as:

$$\text{SPL} = 20 \log_{10}\left(\frac{p'_{\text{rms}}}{p_{\text{ref.}}}\right), \tag{6}$$

where p'_{rms} is the root mean square of the pressure fluctuations, and the reference pressure, $p_{\text{ref.}}$, is 2×10^{-5} Pa.

Positive and negative ΔSPL are, respectively, indicative of constructive and destructive interference between direct source and reflections, at the measurement location. $\Delta\text{SPL} = 0$ indicates that, at that specific frequency, the measurement inside the test section is not disturbed by reflections. The main assumptions are that the reference speaker measurement is representative of free-field conditions; and that the speaker's response is consistent throughout all the tests.

2.4.1. Conventional beamforming

The experimental and simulated acoustic data from the microphone array were processed with conventional frequency domain beamforming. Conventional Beamforming (CBF) is a robust and computationally efficient method for identifying sound sources, and for determining source power levels. CBF is a widely used method in aeroacoustic studies [8]. The signals from the microphone array are processed in the frequency domain:

$$\boldsymbol{p}(f) = \begin{pmatrix} p'_1(f) \\ \vdots \\ p'_N(f) \end{pmatrix}, \tag{7}$$

where p'_n is the pressure fluctuation recorded at each microphone, n. N stands for the number of microphones in the array. The propagation of the sound wave is considered in beamforming in the definition of the steering vector, $g_{j,n}$. The steering vector takes into account the sound wave's spherical spreading and phase shift from a scan grid point, j, to a microphone n. $g_{j,n}$ is the Green's function of the sound propagation for a free-field monopole source:

$$g_{j,n \text{ (free–field)}} = \frac{\exp\left(-2\pi i f \Delta t_{j,n}\right)}{\|\boldsymbol{x}_n - \xi_j\|}, \tag{8}$$
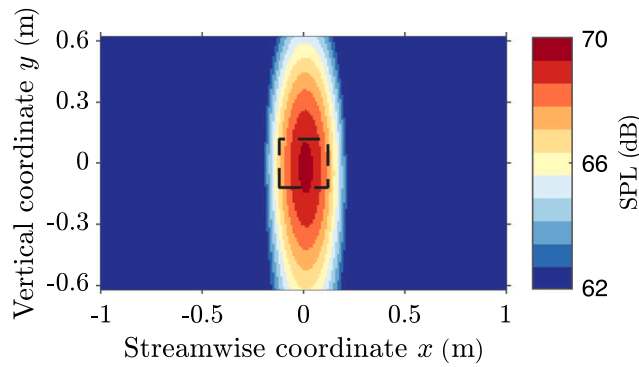
Fig. 6. Beamforming map of the reference speaker measurement, for the $1\,\mathrm{kHz}$ centred third-octave band. Speaker located at a $1.05\,\mathrm{m}$ distance from the array. The $24 \times 24\,\mathrm{cm}^2$ Source Power Integration region is indicated by the dashed line.

where $\Delta t_{j,n} = \left\| x_n - \xi_j \right\| / c$ is the sound propagation time from the grid point location ξ_j to the receiver at x_n. c is the speed of sound. $\| \cdot \|$ is the Euclidean norm of a vector. For the flow-on cases, $\Delta t_{j,n}$ was recalculated taking into account the flow convection of sound waves. The vector x_n contains the coordinates of all microphones in the array. For each grid point, the noise levels are estimated from:

$$A\left(\xi_j\right) = \frac{g_j^*(pp^*)g_j}{\|g_j\|^b}, \tag{9}$$

pp^* is a $N \times N$ matrix, commonly referred to as Cross-Spectral Matrix (CSM), where the asterisk, $(\cdot)^*$, represents the complex conjugate transpose. b is a scalar and is set to 2 or 4, depending, respectively, on whether it is intended to compute the noise levels at the observer (microphone array) or at the source. The diagonal of the CSM, i.e., the auto-powers, has been kept for the processing of the purely acoustic results (flow-off), i.e. the results presented in Sections 3–5, and has been removed for obtaining the results presented in Section 6, relative to the flow-on test cases.

For beamforming, the acoustic data were processed considering a 2D scan grid parallel to the array (see Fig. 6). The 2D grid is at a $1.05\,\mathrm{m}$ distance from the array, and passes through the spanwise centre of the test section, i.e. through the speaker location. After calculating the beamforming maps, the speaker noise levels were obtained with the Source Power Integration (SPI) method [32]. The experimental CSM is normalised with the CSM of a simulated point monopole source, in order to quantify the noise levels of the experimental source:

$$A_{\mathrm{SPI}}(f) = \frac{\sum_{j=1}^{K} A\left(\xi_j\right)_{\mathrm{exp.}}}{\sum_{j=1}^{K} A\left(\xi_j\right)_{\mathrm{sim.}}}, \tag{10}$$

where K is the number of grid points considered in the source power integration. The simulated point source considered in Eq. (10) is a source of unit strength. In the conventional (uncorrected) SPI method, this translates to:

$$A\left(\xi_j\right)_{\mathrm{sim.}} = \frac{g_j^*(g_k g_k^*)g_j}{\|g_j\|^b}, \tag{11}$$

where g_k is the steering vector to the kth grid point, the grid point at the centre of the SPI region.

Fig. 6 shows a beamforming map of the reference speaker measurement. A $24 \times 24\,\mathrm{cm}^2$ SPI region is illustrated. This SPI region was used in this study to estimate the noise levels from the beamforming maps obtained with the free-field Green's function.

For the experimental beamforming maps calculated with a corrected Green's function, a $2 \times 2\,\mathrm{cm}^2$ SPI region was considered. The reason is that correcting the Green's function influences the resolution of the beamforming map. Eq. (10) should not be used for integrating noise levels in regions of the scan plate where the experimental beamforming map (present on the numerator of Eq. (10)) has a different resolution than the simulated beamforming map (present on the denominator of Eq. (10)). This issue can be overcome by simultaneously using the Green's function correction and the SPI correction, both described in the following sub-section.

2.4.2. Corrections to the experimental results

The numerical method described in Section 2.1 was used to model the acoustic behaviour of a source inside closed wind tunnel test sections. The numerical results were used in this study to correct the experimental measurements taken in the LTT, in order to make these acoustic results closer to the reference measurement of the source (the omnidirectional speaker). Two methods were tested for improving the post-processing of experimental data. The first focuses on refining the Green's function used for beamforming (see Eq. (8)). The second is based on changing the denominator of Eq. (10), in this way improving the SPI method.

The reference numerical simulation models a free-field monopole source. Therefore, the propagation in this simulation follows the Green's function described by Eq. (8). However, for the simulations where the wind tunnel test section is present, the propagation of sound is altered. For each numerical simulation, $p'_{s,o}(f)$ is the pressure fluctuation at the observer position o, when the source is
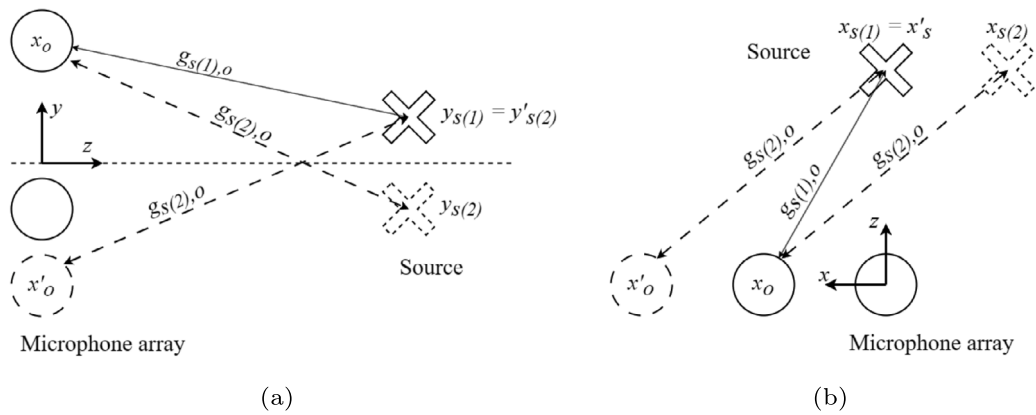
Fig. 7. Method of calculating the Green's function. Mirror with respect to $y = 0$ (a) and assumption that the test section is constant and infinite in the streamwise direction (b).

located at s. $p'_{s,o}(f)$ is complex valued and, therefore, contains both magnitude and phase information. For each o and s, the Green's function of a monopole inside the simulated wind tunnel test section (i.e. in non-free field conditions) is then:

$$g_{s,o \text{ (WT, corrected)}} = g_{s,o \text{ (free–field)}} \frac{p'_{s,o}(f)_{\text{WT simulation}}}{p'_{s,o}(f)_{\text{Ref. simulation}}}. \tag{12}$$

Eq. (12) was used for correcting the Green's function used for post-processing the experimental acoustic measurements with beamforming. This correction requires that the Green's functions of sound propagation in the experimental and numerical wind tunnel setups are equivalent. This is true when the computational modelling of the experimental setup is accurate. The validation of the simulations is discussed in the following Section.

To correct the Green's function, $g_{s,o \text{ (WT)}}$ is calculated for all beamforming scan plane positions. The beamforming map of Fig. 6 was generated for scan plane positions spaced by 0.01 m, i.e. 24 000 positions. The most straight-forward approach for calculating $g_{s,o \text{ (WT)}}$ for the entire scan plane is to perform simulations with the source at each scan plane position. However, this is computationally expensive. Three additional assumptions were made to reduce the number of simulations required. Firstly, the wind tunnel setup was considered to be symmetric in the vertical direction, with respect to the horizontal plane which passes by the source, the plane $y = 0$. In this way, simulations were performed for source locations defined by $y_s \geq 0$. To obtain the value of $g_{s,o \text{ (WT)}}$ for $y_s < 0$, the observer and source's vertical coordinates were instead mirrored: $y'_s = -y_s$ and $y'_o = -y_o$ (see sketch in Fig. 7(a)). This first consideration reduces the number of numerical simulations required to approximately half. Secondly, the test section walls were defined (in the numerical setup) with constant y and z coordinates, leading to a constant test section area with respect to the streamwise direction (whereas the experimental test section walls feature a slight expansion). The simulated test section was also assumed to be infinite, in the streamwise direction. To increase the validity of this assumption, the streamwise test section length was increased in the simulation. As described previously, the test section had been assumed to be symmetric with respect to $x = 0$. Based on these assumptions, it was possible to run simulations exclusively for source positions at the streamwise centre of the test section, $x_s = 0$. To obtain the value of $g_{s,o \text{ (WT)}}$ for $x_s \neq 0$, the observer's streamwise coordinate was instead moved: $x'_s = 0$ and $x'_o = |x_s - x_o|$ (see sketch in Fig. 7(b)). Thirdly, $p'_{s,o}(f)_{\text{WT simulation}}$ and $p'_{s,o}(f)_{\text{Ref. simulation}}$ were assumed to vary linearly, for relatively short variations of the source's vertical position. The simulations were done for source locations spaced by $\Delta y_s = 0.04$ m. For scan plane locations at a vertical location which had not been simulated, $p'_{s,o}(f)_{\text{WT simulation}}$ and $p'_{s,o}(f)_{\text{Ref. simulation}}$ were estimated by linear interpolation. With this approach, it is possible to obtain $g_{s,o \text{ (WT)}}$ for the scan plane seen in Fig. 6 by simulating the source at 16 different locations, instead of 2400. In the present study, the computational cost was further decreased by reducing the scan plane to $0.8 \times 0.32 \text{ m}^2$.

The second correction validated in this study was a correction to the SPI method. This was implemented by correcting the denominator in Eq. (10):

$$A\left(\xi_j\right)_{\text{sim., correction}} = \frac{g^*_{j\text{(free–field)}}(pp^*)_{\text{FEM}} g_{j\text{(free–field)}}}{\|g_{j\text{(free–field)}}\|^b}, \tag{13}$$

where $(pp^*)_{\text{FEM}}$ is the cross-spectral matrix calculated from the numerical acoustic data. Considering the properties of the logarithmic function, the corrected SPI for a source inside the test section can equivalently be calculated from:

$$\text{SPL}_{\text{SPI corr.}} = \left(\text{SPL}_{\text{WT}}\right)_{\text{SPI, Exp.}} - \left(\text{SPL}_{\text{WT}}\right)_{\text{SPI, FEM}}. \tag{14}$$

In this study, each correction was tested separately, i.e., the SPI correction was applied to process beamforming data obtained with the free-field Green's function. This was done to evaluate the benefits from the two correction methods separately. The two

Fig. 8. Summary of the methodology proposed, for using FEM simulations to improve the post-processing of experimental acoustic data collected in a disturbed environment. The black and blue arrows refer to the two approaches suggested and validated in this paper. (For interpretation of the references to colour in this figure legend, the reader is referred to the web version of this article.)

corrections may, however, be used simultaneously, which can be beneficial when the SPI area is relatively large, as previously mentioned.

2.4.3. Summary of the proposed approach

The diagram of Fig. 8 summarises the methodology proposed in this paper for improving the post-processing of experimental acoustic data obtained in a disturbed environment, e.g., a closed test section wind tunnel. The numerical FEM setup is discussed in Section 2.1, and the acoustic wind tunnel experimental setup is described in Section 2.3. The measurement (or extraction) of the pressure fluctuations from the FEM results is discussed in Section 2.4.2, along with the calculation of the corrected Green's function. The beamforming and (uncorrected) SPI methods are introduced in Section 2.4.1. The correction to the SPI method is described in Section 2.4.2.

The two alternative paths tested in this study (black and blue paths in Fig. 8) represent, respectively, the proposed Green's function correction and the proposed SPI correction. The dashed lines suggest possible alternatives to the methodology validated in this paper.

Fig. 9. Grid dependence study of the FEM simulations: spectra of the Baseline test section A (a); spectra of the lined configuration B (b); and overall noise level, for both test sections (c). Spectra obtained from Source Power Integration of the conventional beamforming maps, within a $24 \times 24 \, \text{cm}^2$ region. The overall noise level is obtained from the SPI spectra, considering frequencies in the range $300 \, \text{Hz} \leq f \leq 2000 \, \text{Hz}$, with steps of $\Delta f = 20 \, \text{Hz}$. ΔSPL as defined in Eq. (5).

3. Validation

3.1. Grid dependence study

Fig. 9 shows the results from the grid dependence study of the FEM simulations. Results are shown for the baseline test section (A) and for one of the lined configurations (B). For each test section, three simulations with increasing grid refinement were carried out (grids previously described in Section 2.1.2). The fine grid simulations were computed for fewer frequencies, by setting $\Delta f_{\text{Fine}} = 20 \, \text{Hz}$. For the baseline test section, the numerical calculations with the medium and fine grids had equivalent results (Fig. 9(a)), while differences are visible for the coarse one. For the lined test section, it can be seen that the spectra matches for all three grids (Fig. 9(b)).

The dependence of the overall noise levels with respect to grid refinement is shown in Fig. 9(c). The quantity analysed, p'_i, is obtained by integrating the noise levels shown in the spectra of Figs. 9(a) and 9(b), for each grid resolution i. The convergence of p'_i is analysed with respect to the relative cell size between each grid and the fine resolution grid, h_i/h_{fine}. Based on the lined test section results, p'_i is not expected to vary from the coarse grid to a grid with finer resolution, i.e., with h_i/h_{fine} approximating 0. For the baseline test section, Fig. 9(c) highlights the large difference in result between the coarse grid and the remaining grids.

Based on the results of Fig. 9, the resolution of the coarse grid was deemed sufficient to simulate the lined test sections. For the baseline test section, however, it was concluded that the medium resolution had to be used. For the simulations with a reduced number of walls, the medium refinement was also selected.

3.2. Reflections throughout the wind tunnel circuit

The simulations of the acoustic behaviour of a source inside the wind tunnel were made by modelling the test section. However, this approach does not account for possible contamination caused by reflections in the remaining sections of the wind tunnel circuit.
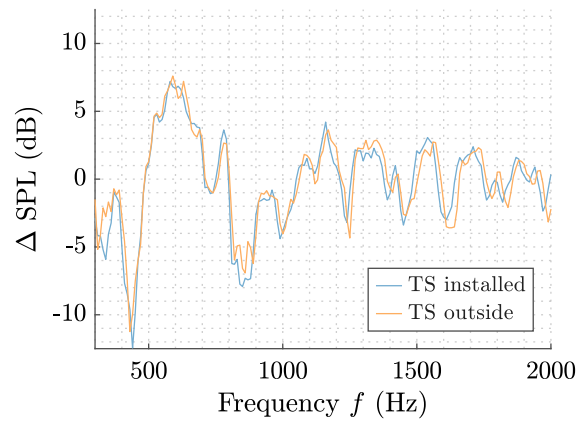
Fig. 10. Acoustic interference caused by the reflections: difference between the measurement inside the test section and the reference speaker measurement. Comparison between installed and uninstalled test section, from experimental data, for test section C. Spectra obtained from Source Power Integration of the conventional beamforming maps, within a $24 \times 24 \, \text{cm}^2$ region.

In order to quantify this disturbance, an additional acoustic test was made. One of the lined test sections (test section C) was removed from the wind tunnel circuit, and placed in a large room, where reverberation is negligible. The reverberation in this room and in the LTT circuit was quantified and discussed in more detail in Ref. [23]. The acoustic measurements conducted with test section C installed in the wind tunnel circuit and placed outside the circuit were compared. The results are shown in Fig. 10. The resulting spectra show negligible differences between the two cases. This indicates that, when the experimental phased-array data is processed with beamforming, the reflections in the wind tunnel circuit, outside of the test section, have a negligible influence in the resulting spectra. Therefore, it is assumed sufficient to model the test section, with the numerical acoustic solver.

3.3. Validation of the FEM simulations

To validate the FEM numerical method, the simulated acoustic spectra were compared against the experimental ones. The comparison was done for the test cases with the monopole acoustic source inside each of the four test sections. The experimental data from test section C was obtained with and without the Kevlar wall placed in front of the microphone array, as discussed in Section 2.3.3. During the experimental measurements with test sections A, B and D, the Kevlar panel remained installed. The spectra were obtained from SPI of the conventional beamforming maps. Fig. 11 shows the results. These spectra were calculated with a $24 \times 24 \, \text{cm}^2$ SPI region, although the spectra calculated with a smaller integration region, of $2 \times 2 \, \text{cm}^2$, are identical.

The agreement between experiment and simulation is very good for all test cases, for frequencies above $500 \, \text{Hz}$. At lower frequencies, the agreement is poorer due to differences between the experimental and numerical setups, which are associated with the assumptions previously discussed in Section 2.3. Fig. 11(c) shows that the Kevlar panel is partially responsible for this difference between experiment and simulations at lower frequencies. The result appears to deviate from results reported in literature, where the acoustic transmission loss through Kevlar, without a grazing boundary layer, is shown to be negligible below $2 \, \text{kHz}$ [3]. This deviation is assumed to be due to the finite size of the Kevlar sheet and of the tunnel opening where it is installed (see Fig. 4). This non-ideal installation causes an increase of the acoustic disturbance at $f < 500 \, \text{Hz}$, where diffraction is a relevant phenomenon (see discussion of Section 4.2). Due to the challenging comparison between experiments and simulations at low frequencies, the methodology proposed in this paper for improving the post-processing of experimental data based on the FEM results is applied for $f \geq 500 \, \text{Hz}$ (results of the improved methodology presented in Sections 5 and 6).

Fig. 11 also shows that the best agreement between experiment and simulation was found for test section B (Fig. 11(b)). As mentioned in the previous section, this is the case for which the lining was most accurately modelled in the simulation: the side panels' wedged-melamine lining was simplified to flat melamine lining, for simulating test sections C and D (Figs. 11(c) and 11(d)). Fig. 11(a) shows that the simulation of the baseline section captures sharper acoustic interference peaks than seen in the experimental result, possibly explained by the limited experimental measurement time (detailed in Section 2.4).

4. Key acoustic phenomena

The present section identifies the dominant acoustic phenomena which occur inside the octagonal LTT test section. Section 4.1 discusses the significance of mirror reflections in the test section, Section 4.2 describes the disturbance caused by diffraction on the test section's acoustic response, and Section 4.3 analyses the acoustic absorption which occurs in the lined configurations.
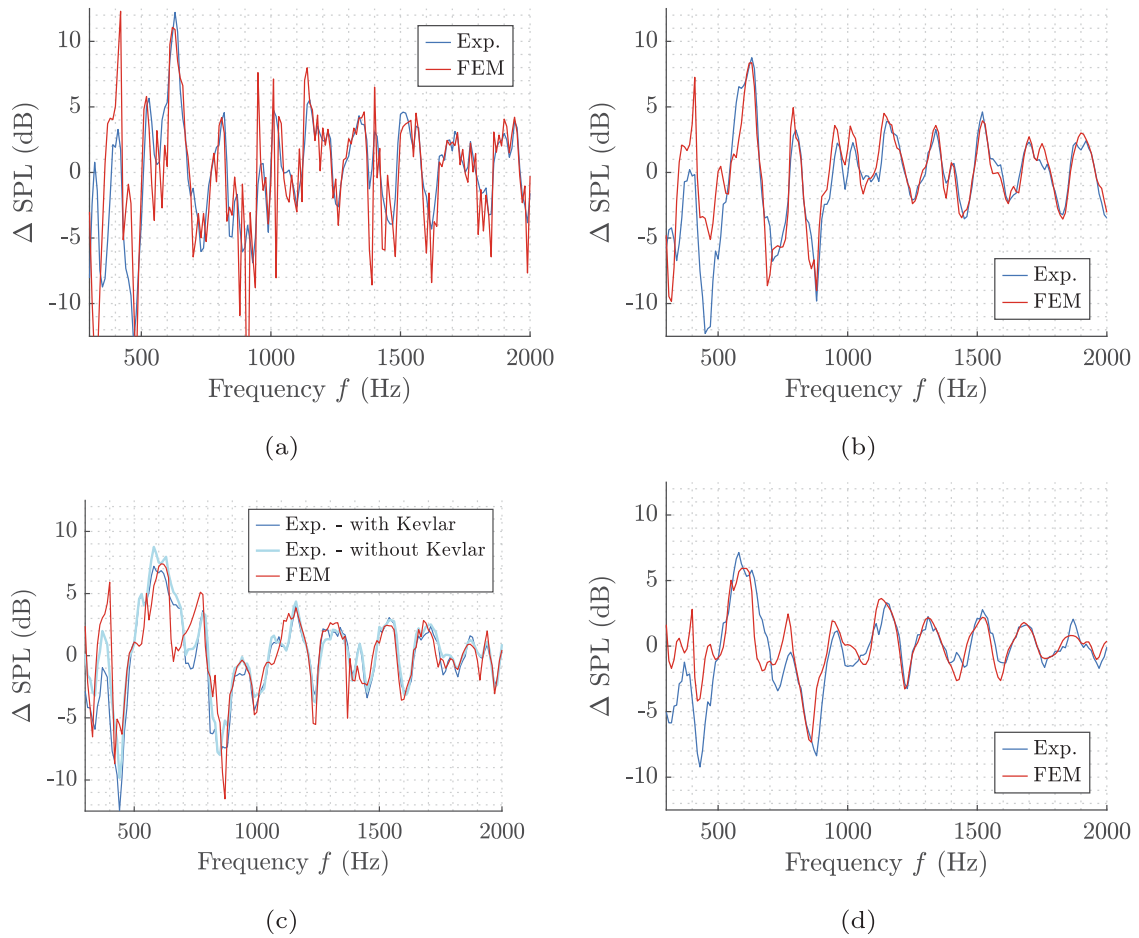
Fig. 11. Validation of the numerical acoustic simulations. Comparison between the simulated and experimental spectra, for the test cases with a monopole source at the centre of each test section: baseline test section A (a); lined test section B (b); lined test section C (c); and lined test section D (d). Spectra obtained from Source Power Integration of the conventional beamforming maps, within a $24 \times 24\,\text{cm}^2$ region.

4.1. Mirror reflections

The relevance of mirror reflections on the acoustic interference at the microphone array location was analysed by simulating a reduced number of test section walls, both with the FEM solver and with the geometric modelling algorithm. The acoustic interference results, obtained from beamforming of the synthetic data, are shown in Fig. 12. Fig. 12(b) shows that the reflections on the floor and opposite wall can be modelled by considering three mirror sources, i.e. by including the secondary reflection. The result shows that, for the two walls' setup (see Fig. 12(a)), specular reflections are dominant with respect to diffraction at the wall edges and at the corner between the two walls. The spectra shown in Fig. 12(c) indicates that the tertiary reflections should also be modelled for predicting the disturbance caused by specular reflections, in the three walls case.

This GM algorithm does not account for diffraction and diffuse reflections, thus it can only approximate the behaviour of the three main walls of the LTT test section. However, the FEM spectrum shown in Fig. 12(c) (3 main LTT walls) is considerably different from the spectra of Fig. 11(a), i.e., the spectra for the baseline LTT test section. This indicates that the mirror source-method is insufficient for accurately predicting the acoustic response of the LTT's test section, even if an infinite number of mirror reflections is considered.

4.2. Diffraction

The present section analyses the disturbance caused by acoustic diffraction inside the LTT test section. This effect is visible in Fig. 13, where the acoustic fields of the two walls FEM simulations are shown, for the frequencies $f = 500\,\text{Hz}$ and $f = 2000\,\text{Hz}$. The acoustic fields are taken at the $x = 0$ plane, from the FEM simulations. The two walls' acoustic fields are compared with the case where a 45° angled edge is added to the floor wall, close to the array (see Figs. 13(b) and 13(e)), and to the case where a 45° angled corner is added, between the floor and the wall opposite to the array (see Figs. 13(c) and 13(f)). In the test cases analysed
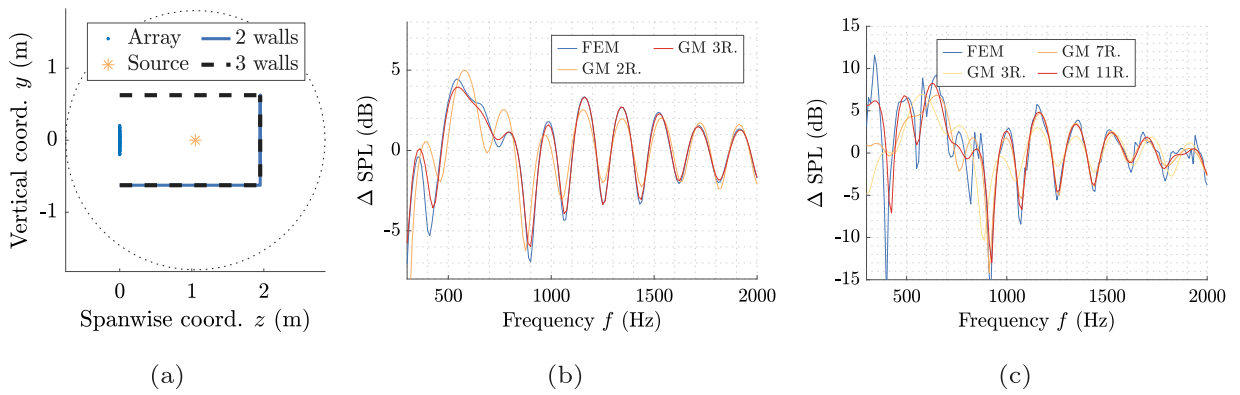
Fig. 12. Acoustic interference caused by specular reflections in the (fully reflective) test section, simplified to a reduced number of walls. Simulation setup (a), and comparison between FEM and geometric modelling of the two walls (b) and three walls (c) cases. Spectra obtained from Source Power Integration of the beamforming maps of the simulated data, within a $24 \times 24 \, \text{cm}^2$ region.
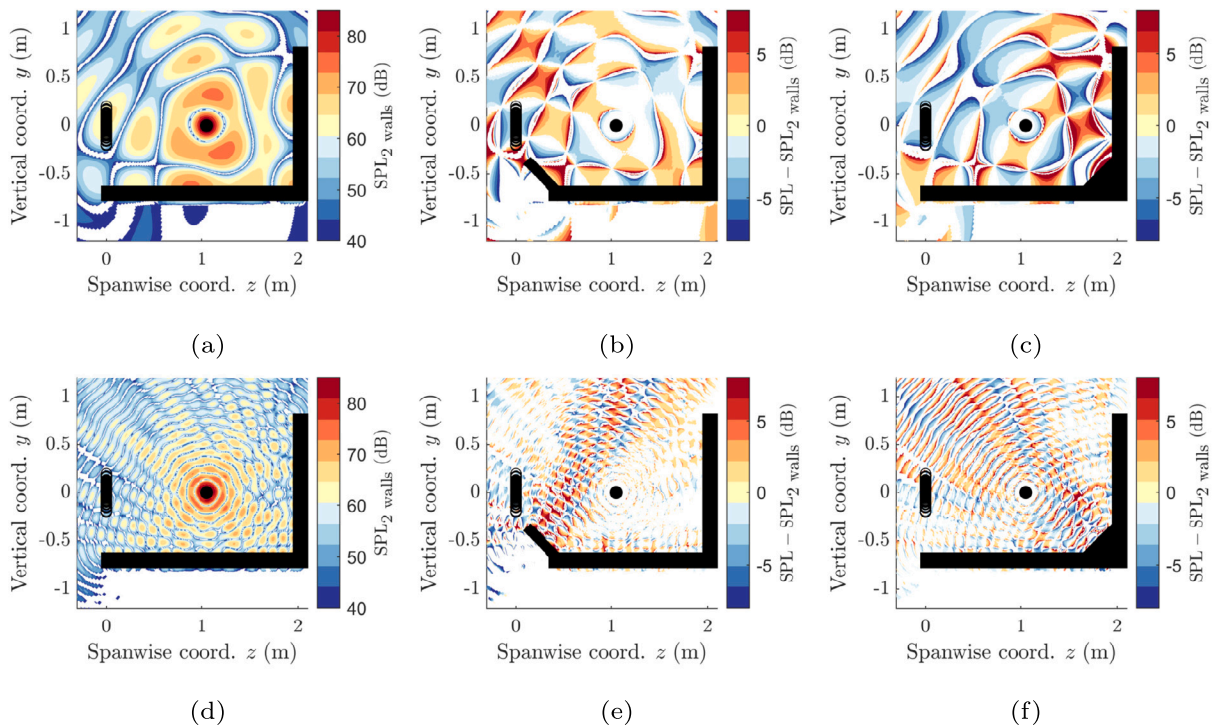
Fig. 13. Acoustic fields of the test cases with the floor and with the wall opposite to the array. Simulations of the: 2 walls case (a), (d); 2 walls with an angled edge (b), (e); and 2 walls with the angled corner (c), (f). Calculations with the source emitting noise: at 500 Hz (a), (b), (c); and at 2000 Hz (d), (e), (f). Acoustic fields at the $x = 0$ plane, obtained from the Finite Element Method simulations. $\text{SPL}_{2 \, \text{walls}}$ is the acoustic field of the 2 walls case, which in this figure is considered as reference.

in the previous sub-section (Fig. 12), each wall could be substituted by its mirror reflections. However, the additional angled edge and corner, which are part of the LTT test section, cannot be simulated with a geometric modelling algorithm (either the mirror source method or ray tracing), as there is no direct path from the primary reflections on these walls to the microphone array.

Figs. 13(b) and 13(c) show that, at $f = 500 \, \text{Hz}$, the primary reflections on the angled walls lead to a considerable disturbance in the entire acoustic field. Acoustic diffraction leads to the propagation of reflected waves to locations for which there is no direct specular reflection path, including to the microphone array location. This is also a strong indication that, at low frequency (e.g. 500 Hz), the LTT test section's acoustic response cannot be modelled with a (lower fidelity) geometric modelling algorithm. Figs. 13(e) and 13(f) show that, at higher frequency, reflections on the angled walls become closer to what can be predicted with geometric modelling, i.e. by drawing the specular reflections path.
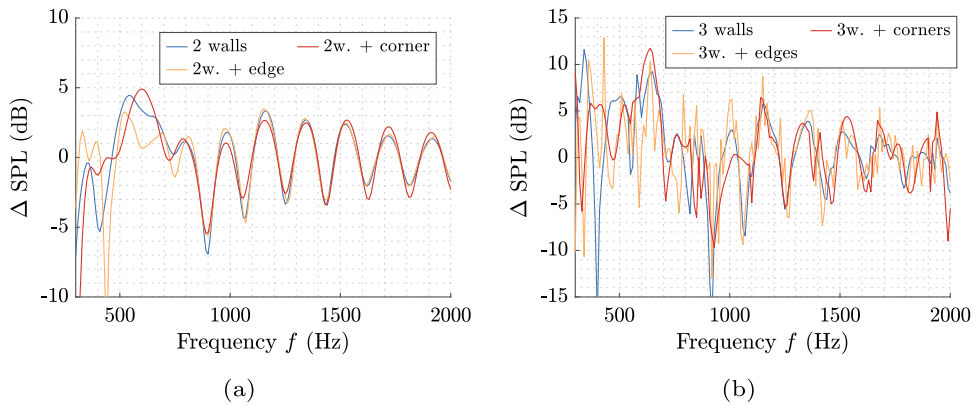
Fig. 14. Acoustic interference caused by specular reflections in the (fully reflective) test section, simplified to a reduced number of walls. Comparison between the baseline 2 walls (a) and 3 walls (b) cases and the cases where angled edges and corners are added to the FEM setup. Spectra obtained from Source Power Integration of the beamforming maps of the simulated data, within a $24 \times 24 \, \text{cm}^2$ region.

Fig. 14 quantifies the change which occurs in the SPI spectra by adding the angled edges and corners to the two and three walls test cases. Fig. 14(a) shows that, for the 2 walls case, the disturbances caused by the edge and corner are limited to low frequencies, $f < 1000 \, \text{Hz}$. For the 3 walls case, the number of reflections which reach the array becomes infinite, and the disturbance caused by edges and corners increases. For this reason, the spectra in Fig. 14(b) are dissimilar for all frequencies analysed. Still, the highest differences with respect to the baseline 3 walls case are found for low frequencies, i.e., for $f < 1000 \, \text{Hz}$, where diffraction is more relevant.

4.3. Wave absorption by lining

Fig. 15 shows the acoustic field inside each test section, with the simulated source emitting noise at the frequency $f = 1000 \, \text{Hz}$. Fig. 15(a) indicates that, inside the baseline test section, the sound wave pattern is largely dominated by specular reflections. In the region where the microphones are placed, the waves appear to display a curvature around the test section opening, highlighting the importance of sound diffraction. Figs. 15(b)–15(d) show the difference in acoustic field between each lined test section and the baseline configuration. The figures clearly show that, as the lining over the walls is increased, the acoustic energy inside the test section is reduced. However, lining the test section walls also changes the acoustic interference pattern. For this reason, there are also locations inside each of the lined test sections where acoustic energy at $f = 1000 \, \text{Hz}$ is higher than for the baseline case. This result highlights the need to accurately model reflections inside each lined test section, e.g., with a high fidelity numerical tool, as demonstrated in this paper.

5. Improvements to the beamforming technique

5.1. Source identification with beamforming

The improvement of beamforming resolution in an environment disturbed by reflections, by correcting the (free-field) Green's function, is evaluated for the beamforming formulations with $b = 2$ and $b = 4$ (see Eq. (9)). Fig. 16 shows the beamforming maps calculated from numerical data, correspondent to the simulation of a source inside test section B (lined floor and ceiling). The maps were obtained with the $\|g\|^2$ beamforming formulation, i.e. with $b = 2$. The maps calculated with the uncorrected free-field Green's function are shown in Figs. 16(a)–16(c), whereas the maps obtained with the corrected Green's functions are shown in Figs. 16(d)–16(f). The results show a clear increase in beamforming resolution in the vertical direction. The reason for the high increase in resolution in the vertical direction is that the noise source inside the test section is aligned with its mirror reflections in the same direction (floor and ceiling reflections). The increase in resolution is noticeable for all frequencies tested.

The beamforming data of Fig. 16, at the source plane lines $x = 0$ and $y = 0$, can be analysed in more detail with Fig. 17. The figure clarifies that there is a strong increase in resolution in the vertical direction, whereas the resolution in the streamwise direction sees a negligible change when the Green's function is corrected. The streamwise resolution does not improve with this correction since all simulated tunnel walls are parallel with the streamwise direction vector, i.e., there is no mirror source that can be placed at a different streamwise location than the source, for describing the acoustic problem.

The beamforming of microphone data from the simulation of a monopole at the centre of test section B, with the $\|g\|^4$ beamforming formulation, is shown in Fig. 18. For high frequencies, these results also show an increase in beamforming resolution when the corrected Green's function is used. However, the formulation with $\|g\|^4$ leads to higher side-lobes in the beamforming map. Fig. 18(d) shows that, for the third-octave band centred at $f_{\text{center}} = 500 \, \text{Hz}$, the side-lobes' noise levels are higher than the noise levels of the primary source. At $f_{\text{center}} = 500 \, \text{Hz}$, it is therefore impossible to identify the noise source, when the correction is
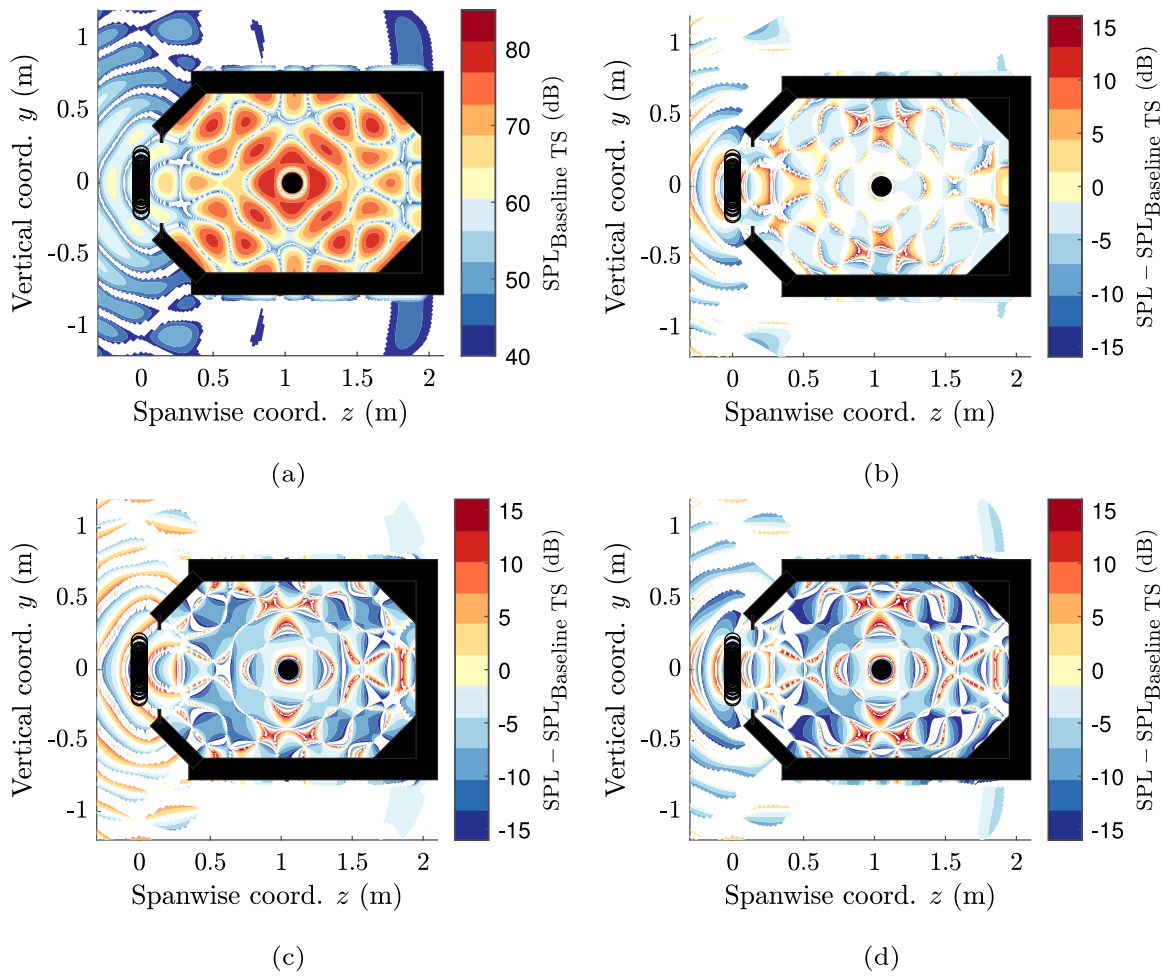
Fig. 15. Acoustic field inside each of the LTT test sections: baseline section A (a); test section B, with lining on the floor and ceiling (b); test section C, with lined side–panels (c); and fully lined test section D (d). Calculations with the source emitting noise at 1000 Hz. Acoustic fields at the $x = 0$ plane, obtained from the FEM simulations. $SPL_{Baseline\ TS}$ is the acoustic field of the baseline test section (a), which in this figure is considered as reference.

used. This does not occur for the beamforming map with the free-field Green's function. Fig. 18 therefore shows the disadvantage of the $\|g\|^4$ beamforming formulation for processing acoustic data measured in a disturbed environment. The finding is in agreement with the results presented in Ref. [33], where similar Green's functions were implemented (formulations I and II of Ref. [33]) for localising an isolated source in an undisturbed environment, within a three-dimensional beamforming scan plane. In Ref. [33], formulation II of the Green's function, which is equivalent to the formulation with $\|g\|^4$ in this study, was shown mathematically to not lead to a local maximum at the physical location of the source, in the beamforming map.

As the beamforming formulation with $\|g\|^2$ is found to provide a more accurate source localisation, this formulation was used to localise the noise source in the experimental data. Test section B is the case for which the numerical simulations give the best agreement with experiments (see discussion of Fig. 11), and is therefore the case analysed in Fig. 19. The figure compares the beamforming maps of the free-field case with the beamforming map of the omnidirectional source inside the lined test section. For the free-field test case, the figure shows both the beamforming Point Spread Function (PSF) of the free-field Green's function and the beamforming maps of the experimental reference measurement. This figure clearly shows that the proposed methodology is capable of increasing beamforming resolution during the post-processing of experimental data in a disturbed environment. The increase in resolution is observed in the direction where the direct source is aligned with its mirror reflections, i.e., the vertical direction, in this case.

5.2. Determination of the source power levels

The Green's function correction is shown to improve source localisation with beamforming. Simultaneously, it is important to evaluate the accuracy of the estimate of the source levels, when the correction is used. The error in source level's estimation, when
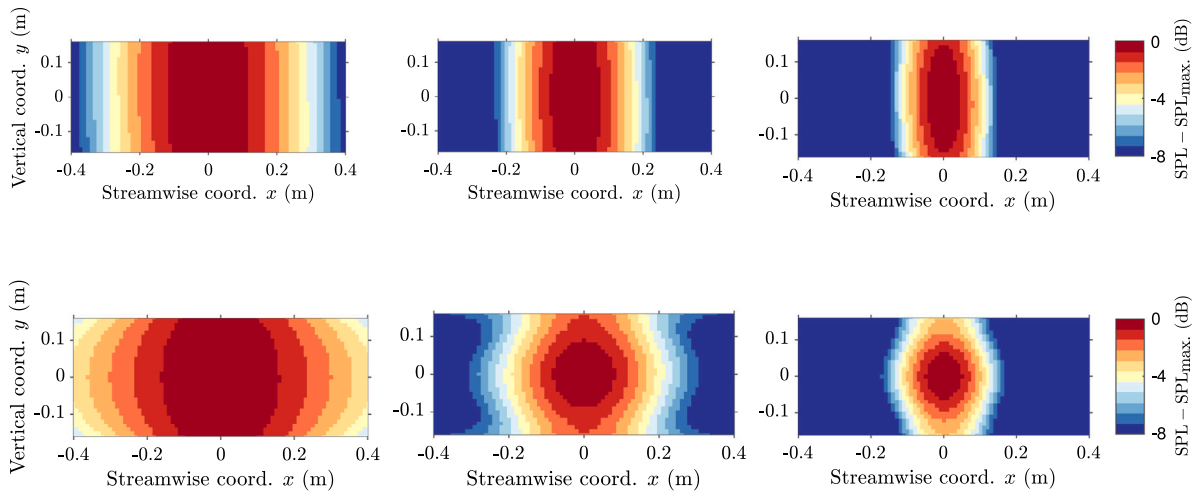
Fig. 16. Beamforming maps obtained from the simulation of a source at the centre of test section B, which is lined on the floor and ceiling. Beamforming with: the free–field Green's function (a), (b), (c); and with the corrected Green's function (d), (e), (f). Third-octave bands centred: at 630 Hz (a), (d); at 1000 Hz (b), (e); and at 1600 Hz (c), (f). Maps calculated with the $\|g\|^2$ beamforming formulation.
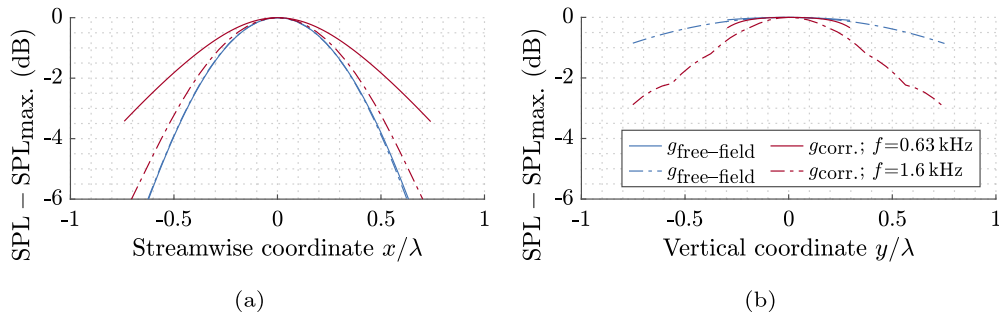
Fig. 17. Resolution of the beamforming maps obtained with the free-field and with the corrected Green's functions. Resolution: in the streamwise direction (a); and in the vertical direction (b). Synthetic data from the FEM simulation of a source at the centre of test section B. Results shown for the third-octave frequency bands centred at $f_{center} = 630$ Hz and $f_{center} = 1600$ Hz.

using the free-field Green's function, can be seen in Fig. 11. The spectra obtained with the corrected Green's functions, for each test section, is shown in Fig. 20. As mentioned previously, ΔSPL(f) = 0 represents a noise level estimation equal to the noise level calculation from the reference measurement, i.e., ΔSPL(f) = 0 indicates a correct estimation. The figure shows that, when the $\|g\|^4$ beamforming formulation is used, there is a significant improvement in the noise levels calculation. However, when the Green's function formulation with $\|g\|^2$ is used, the source's noise levels estimation does not visibly improve with respect to the estimation with the free-field Green's function. This occurs because, with $\|g\|^2$, the beamforming result indicates the noise levels at the microphone array, where reflections are also included. The formulation with $\|g\|^4$ instead corrects for the acoustic interference which disturbs the measurement, and is able to provide an estimation of the noise levels without the reflections.

Fig. 20 also shows the spectra obtained using the SPI correction. For the baseline test section, Fig. 20(a) shows that the Green's function correction outperforms the SPI correction. This is associated with the sharp acoustic interference peaks seen for the numerical calculation with the source at the centre of the baseline test section, which did not occur in the experiment (see Fig. 11(a)). As the corrected Green's function is obtained with simulations at varying source location, the presence of these sharp interference peaks in the corrected result is mitigated. For the lined test sections (Figs. 20(b)–20(d)) the SPI correction provides the same improvement as the use of the Green's function formulation, with $\|g\|^4$. This reveals an advantage of the SPI correction. This correction only requires a single numerical simulation for each test section, whereas correcting the Green's function requires several numerical computations. A main advantage of the Green's function correction, for the purpose of source noise levels calculation, is that this correction does not require a priori knowledge of the source location. For an experimental acoustic environment which is perfectly described by the computational model, both corrections are expected to lead to precise source noise level estimations.

Fig. 20 also reveals that the corrected ΔSPL closest to 0 occurs for test section B. The lining on this test section clearly provides lower sound absorption than the lining on the remaining test sections (see Fig. 15). However, as shown in Fig. 11, the floor and ceiling flat melamine lining were the most accurately modelled liners. The result of Fig. 20 clearly indicates that, for experimental
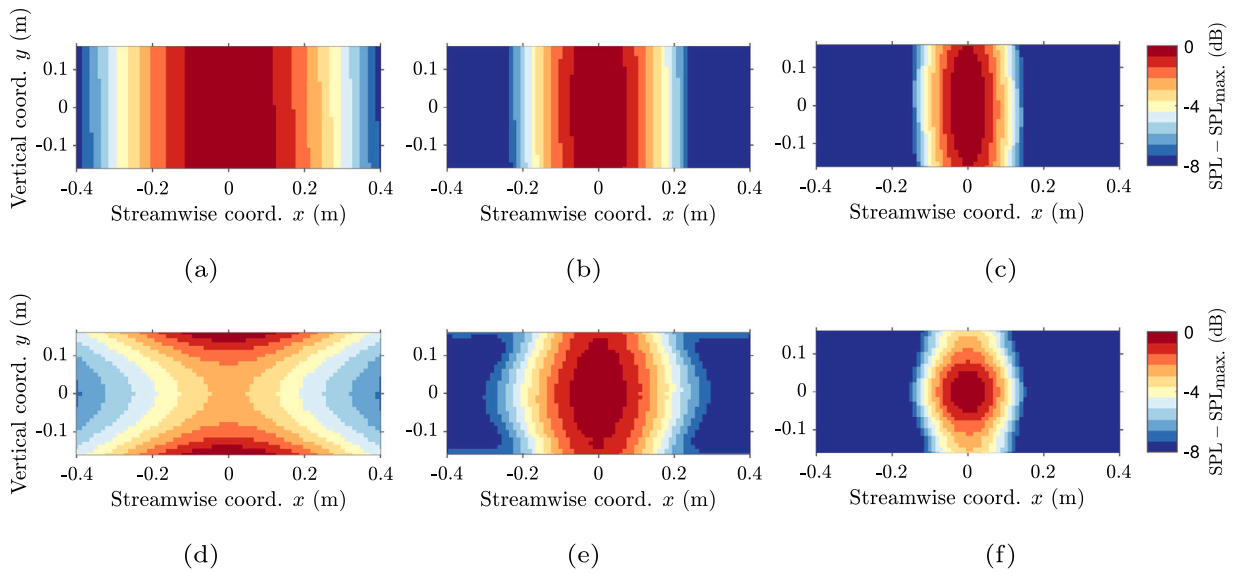
Fig. 18. Beamforming maps obtained from the simulation of a source at the centre of test section B, which is lined on the floor and ceiling. Beamforming with: the free-field Green's function (a), (b), (c); and with the corrected Green's function (d), (e), (f). Third-octave bands centred at: at 630 Hz (a), (d); at 1000 Hz (b), (e); and at 1600 Hz (c), (f). Maps calculated with the $\|g\|^4$ beamforming formulation.
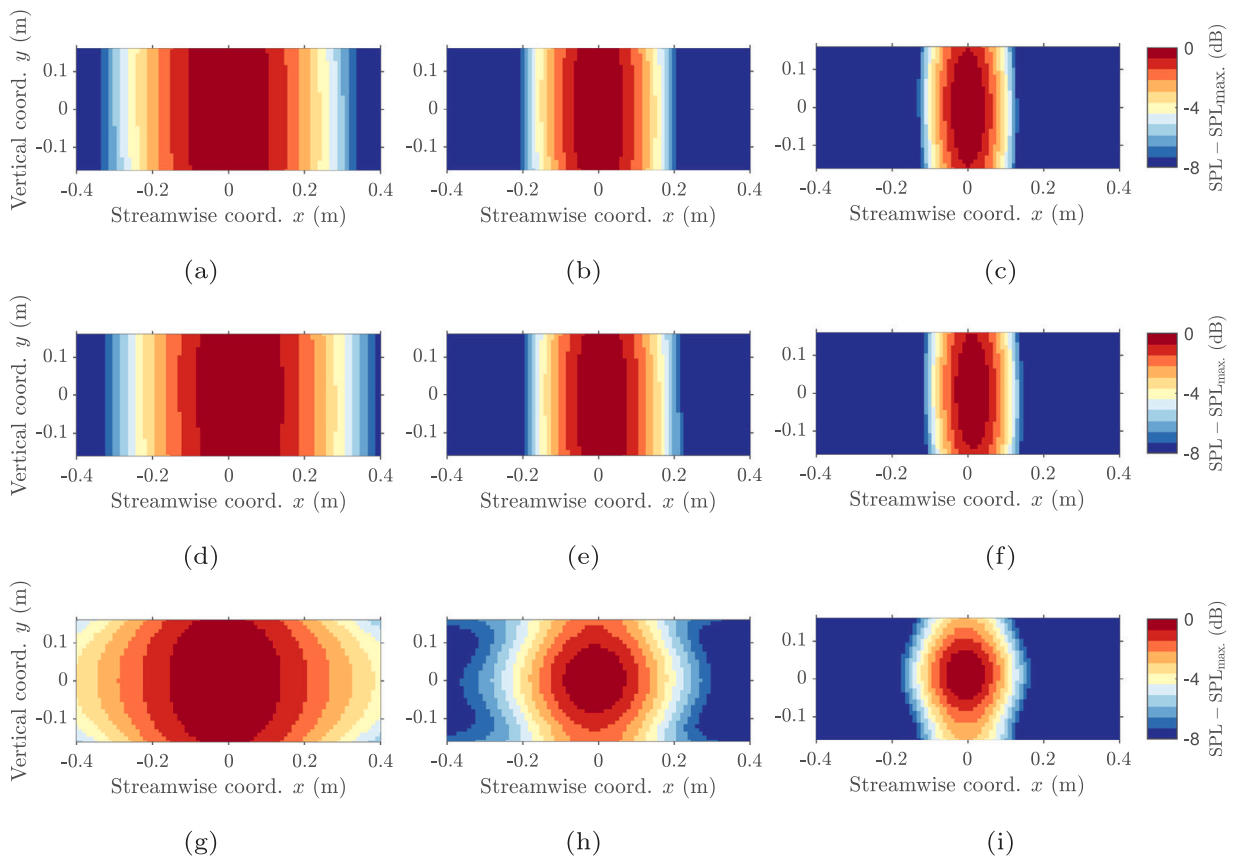
Fig. 19. Point Spread Function of the microphone array, calculated with the free-field Green's function (a), (b), (c). Beamforming maps obtained from the experimental measurements of a source: in an environment with low reverberation (d), (e), (f), calculated with the free-field Green's function; and at the centre of the lined test section B (g), (h), (i), calculated with the corrected Green's function. Third-octave bands centred: at 630 Hz (a), (d), (g); at 1000 Hz (b), (e), (h); and at 1600 Hz (c), (f), (i). Maps calculated with the $\|g\|^2$ beamforming formulation.
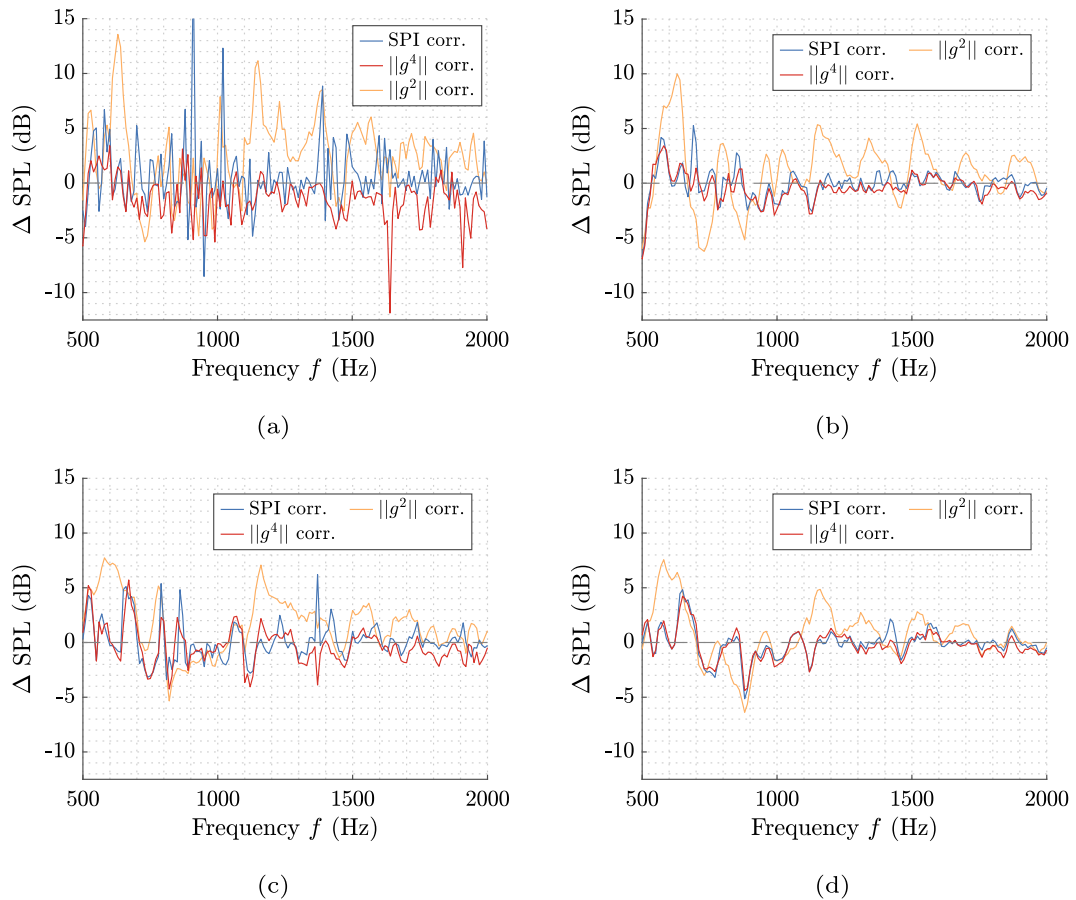
Fig. 20. Spectra of the experimental measurements of an acoustic monopole source at the centre of each test section, improved with the Source Power Integration correction and with the Green's function corrections. Acoustic signals measured with the: baseline test section A (a); lined test section B (b); lined test section C (c); and lined test section D (d). Spectra obtained from Source Power Integration of the beamforming maps, within a $24 \times 24 \, \text{cm}^2$ region (SPI correction) and a $2 \times 2 \, \text{cm}^2$ region ($\|\boldsymbol{g}\|^2$ and $\|\boldsymbol{g}\|^4$ corrections).

acoustic measurements corrected with numerical data, it is important to perform an accurate characterisation of the lined walls. This characterisation needs to be precise both in terms of the lining material, here described based on its viscous resistivity, and liner shape. This study also reveals that too strong acoustic reflections increase the challenge of matching experiment and simulations, i.e., lining a wind tunnel's test section allows for more accurate numerical predictions and consequent corrections.

6. Application of the post-processing methodology to flow-on test cases

The previous results show that the most accurate acoustic predictions have been made for test section B, where the floor and ceiling of the wind tunnel are lined. The applicability of the proposed post-processing method to flow-on test cases is therefore analysed with this test section. Fig. 21 shows the beamforming maps of the data obtained from the measurements of the speaker emitting broadband noise (signal description in Section 2.3.2), with a free-stream velocity in the test section of $30 \, \text{m s}^{-1}$. Fig. 21(a) shows that, without taking into account the convection of sound in the calculation of the Green's function, the speaker's streamwise location in the beamforming map is approximately $0.15 \, \text{m}$ downstream of its actual location ($x = 0$). Fig. 21(b) shows that the accuracy of the speaker's location in the beamforming map is improved by correcting for sound convection. However, as in Fig. 21(b) the correction for the sound reflections is not yet applied, the resolution of beamforming is relatively low (in agreement with the previous discussion, of Section 5.1). Fig. 21(c) proves that, when both corrections are applied simultaneously, it is possible to correct the streamwise location of the source in the map and at the same time improve beamforming resolution.

It is relevant to note that the correction for the reflections was obtained without considering convection of sound in the FEM model. The correction method is therefore applicable to low free-stream Mach numbers, M_∞. $U_\infty = 30 \, \text{m s}^{-1}$ corresponds to $M_\infty = 0.09$. Ref. [23] proposes the use of the mirror source method to analyse if M_∞ is large enough to significantly modify the acoustic interference pattern at a microphone array location. Based on the results presented in Ref. [23], it was expected that the post-processing methodology proposed in this study would be applicable to acoustic data measured at $M_\infty = 0.09$, but not to data measured with $M_\infty = 0.29$ ($U_\infty = 100 \, \text{m s}^{-1}$) at the LTT.
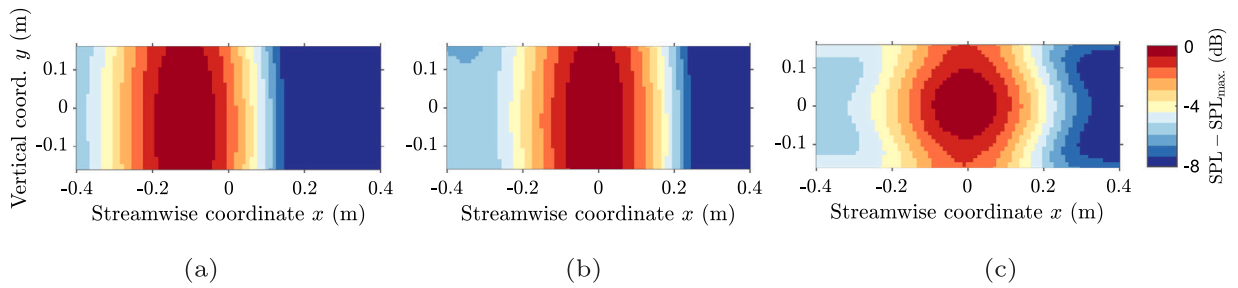
Fig. 21. Beamforming maps obtained from experimental acoustic data measured at the LTT test section B, with $U_\infty = 30\,\mathrm{m\,s^{-1}}$. The speaker was located at the centre of the test section, and emitting broadband noise. Beamforming with the $\|g\|^2$ beamforming formulation and with the CSM diagonal removed. The maps correspond to the third-octave band centerred at $f_{\text{center}} = 1000\,\mathrm{Hz}$. Beamforming with: the free-field Green's function (a); with the Green's function calculated considering convection of sound by the flow (b); and with the Green's function simultaneously calculated considering sound convection and using the numerical (FEM) correction, which takes into account acoustic interference at the microphones (c).

6.1. Determination of the source power levels

Fig. 22 shows the improvement in noise levels estimation by using the SPI and Green's function corrections, when processing flow-on test cases. The spectra in Fig. 22 were calculated considering sound convection in the beamforming formulation (as in Figs. 21(b) and 21(c)). These results were obtained by performing beamforming with the diagonal of the CSM removed. The results at $f < 800\,\mathrm{Hz}$ shown in Fig. 22 correspond to measurements where the speaker was emitting the low frequency narrow band noise, and the results at $f > 800\,\mathrm{Hz}$ correspond to measurements where the speaker was emitting the broadband noise (description of the speaker input in Section 2.3.2). Fig. 22(a) shows, for reference, results for the $U_\infty = 0\,\mathrm{m\,s^{-1}}$ case, processed in the same way as the flow-on cases. The spectra are identical to the spectra shown in Figs. 11(b) and 20(b), confirming that the difference in post-processing technique (removal of the CSM diagonal) does not affect the previous conclusions.

As for the flow-off case, the $U_\infty = 20\,\mathrm{m\,s^{-1}}$ results (Fig. 22(b)) show the SPI and the Green's function corrections leading to similar results. This indicates that both methods can be used when background noise is relatively low.

At $U_\infty = 30\,\mathrm{m\,s^{-1}}$, however, the background noise during the test is noticeable in the resulting beamforming spectra for frequencies $f < 900\,\mathrm{Hz}$. This is indicated by the difference between the $0\,\mathrm{m\,s^{-1}}$ and $30\,\mathrm{m\,s^{-1}}$ uncorrected spectra in Fig. 22(c). Consequently, at $f < 900\,\mathrm{Hz}$, the Green's function correction leads to a better spectra estimation than the SPI correction. Fig. 22(c) demonstrates that the Green's function correction can also be used to improve the signal to noise ratio in the post-processing of experimental data. This is due to the improved spatial resolution of the corrected Green's function, which helps to differentiate the noise source of interest from spurious noise sources.

7. Conclusions

Numerical simulations were carried out for predicting sound propagation in complex-shaped closed wind tunnel test sections. The numerical solver uses a Finite Element Method to solve the Helmholtz equation for acoustic waves. These simulations were validated by comparing the numerical results with acoustic data obtained at the Low Turbulence Tunnel (LTT), a closed section wind tunnel at Delft University of Technology. This validation included a baseline wind tunnel test section, i.e., a test section with fully reflective walls, and lined test sections.

The numerical results show that, along with specular reflections, diffraction is a dominant acoustic phenomenon occurring at the LTT's octagonal test sections. Therefore, the test sections' acoustic response cannot be precisely predicted with lower fidelity methods, e.g., geometric modelling. The numerical results were used to improve the post-processing of experimental acoustic data recorded at the LTT. A corrected Green's function with the $\|g\|^2$ formulation was capable of improving source localisation in the disturbed environment, by enhancing beamforming resolution. Furthermore, both the Source Power Integration correction and the $\|g\|^4$ Green's function correction led to more accurate estimations of the source's noise levels, by reducing the adverse effects of acoustic interference in each disturbed environment. While the uncorrected source noise levels estimation is more accurate for the most lined LTT test section, the noise estimations with the corrections are most accurate for the test section where the liners are most accurately described in the numerical model.

Up to the free-stream Mach number $M_\infty = 0.09$, the post-processing methodology proposed in this study was shown to be applicable to flow-on acoustic tests. For the flow-on test case with a relatively high background noise, the Green's function correction also showed the advantage of improving signal to noise ratio. This is due to an improvement in resolution of the beamforming map, which helps to differentiate between noise sources.

The present study shows the benefits of modelling acoustic propagation in a wind tunnel test section, when studying an omnidirectional noise source. Future studies should extend the proposed numerical prediction to cases with more complex sound sources, e.g., with a dipole directivity and/ or distributed over a line. This will make the method applicable to airfoil noise measurements. Furthermore, it is recommended that numerical acoustic simulations are conducted to support the design of new aeroacoustic wind tunnel test sections, as they can provide an accurate prediction of the facilities' acoustic performance.

(a)

(b)

(c)
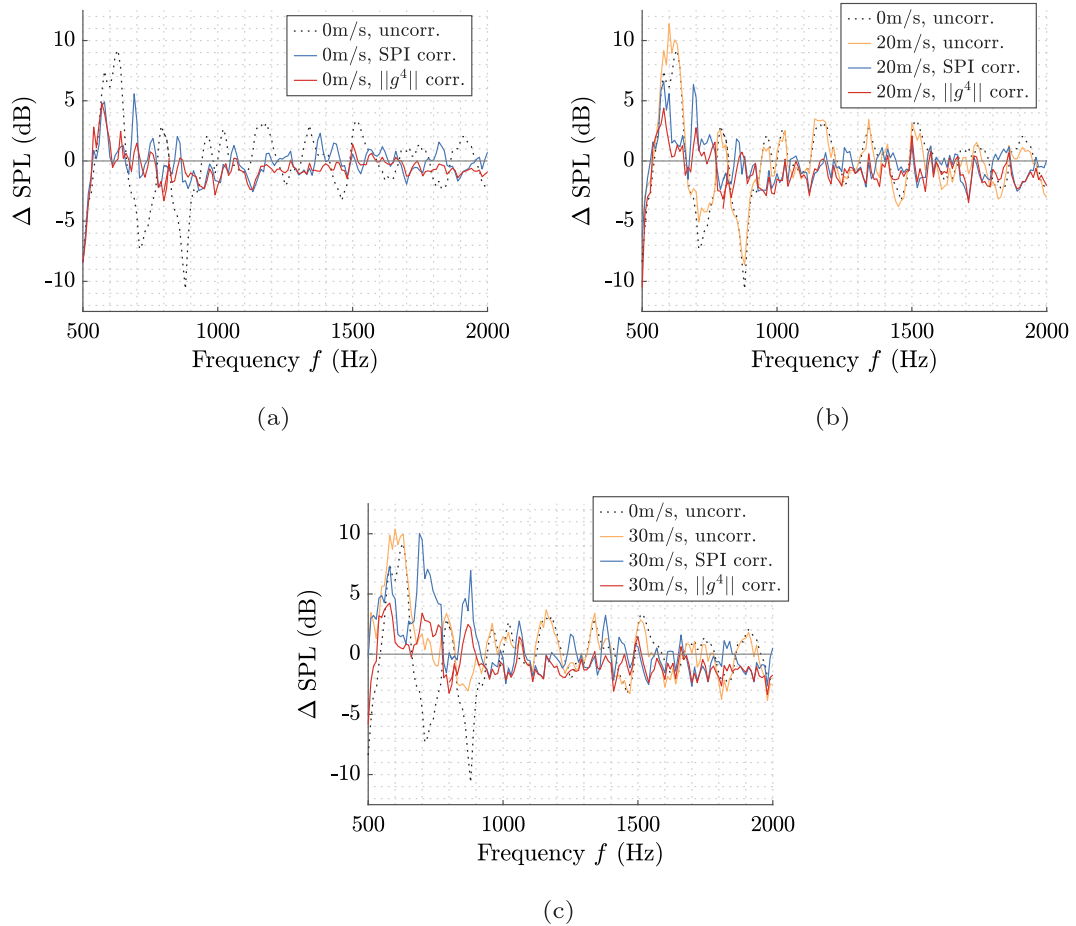
Fig. 22. Spectra of the experimental measurements of an acoustic monopole source at the centre of test section B, at varying free-stream velocity. The lines show the uncorrected spectra, and the spectra improved with the Source Power Integration correction and with the Green's function correction. Acoustic signals measured at: $U_\infty = 0\,\mathrm{m\,s^{-1}}$ (a); $U_\infty = 20\,\mathrm{m\,s^{-1}}$ (b); and $U_\infty = 30\,\mathrm{m\,s^{-1}}$ (c). Sound convection was taken into account in the Green's function calculation, for all results in the figure (taking into account each U_∞). Spectra obtained from Source Power Integration of the beamforming maps, within a $2 \times 2\,\mathrm{cm^2}$ region, and with the $\|g\|^4$ beamforming formulation.

CRediT authorship contribution statement

Hugo F. Mourão Bento: Writing – review & editing, Writing – original draft, Visualization, Validation, Resources, Methodology, Investigation, Formal analysis, Conceptualization. **Colin P. VanDercreek:** Writing – review & editing, Resources, Investigation. **Francesco Avallone:** Writing – review & editing, Supervision, Methodology, Conceptualization. **Daniele Ragni:** Writing – review & editing, Supervision, Methodology, Funding acquisition, Conceptualization. **Pieter Sijtsma:** Writing – review & editing, Methodology, Conceptualization. **Mirjam Snellen:** Writing – review & editing, Supervision, Methodology, Funding acquisition, Conceptualization.

Declaration of competing interest

The authors declare that they have no known competing financial interests or personal relationships that could have appeared to influence the work reported in this paper.

Acknowledgements

Data availability

Data will be made available on request.

References

[1] L. Cattafesta, C. Bahr, J. Mathew, Fundamentals of wind-tunnel design, in: Encyclopedia of Aerospace Engineering, 2010, http://dx.doi.org/10.1002/9780470686652.eae532.

[2] H.F. Mourão Bento, C.P. Vandercreek, F. Avallone, D. Ragni, M. Snellen, Lattice Boltzmann very large eddy simulations of a turbulent flow over covered and uncovered cavities, Phys. Fluids 34 (10) (2022) 105120, http://dx.doi.org/10.1063/5.0100001.

[3] W.J. Devenport, R.A. Burdisso, A. Borgoltz, P.A. Ravetta, M.F. Barone, K.A. Brown, M.A. Morton, The Kevlar-walled anechoic wind tunnel, J. Sound Vib. 332 (17) (2013) 3971–3991, http://dx.doi.org/10.1016/j.jsv.2013.02.043.

[4] D. Blacodon, J. Bulté, Reverberation cancellation in a closed test section of a wind tunnel using a multi-microphone cesptral method, J. Sound Vib. 333 (9) (2014) 2669–2687, http://dx.doi.org/10.1016/j.jsv.2013.12.012.

[5] P.T. Soderman, F.H. Schmitz, C.S. Allen, S.M. Jaeger, J.N. Sacco, J.A. Hayes, Design of a deep acoustic lining for the 40- by 80- Foot Wind Tunnel test section, in: 5th AIAA/CEAS Aeroacoustics Conference and Exhibit, 1999, p. 1938, http://dx.doi.org/10.2514/6.1999-1938.

[6] F. do N. Monteiro, R. Duivenvoorden, D. Ragni, F. Avallone, T. Sinnige, Experimental analysis of synchrophasing impact on noise of distributed propeller systems in tractor configuration, in: 30th AIAA/CEAS Aeroacoustics Conference, Rome, Italy, 2024, p. 3421, http://dx.doi.org/10.2514/6.2024-3421.

[7] C.P. VanDercreek, R. Merino-Martínez, P. Sijtsma, M. Snellen, Evaluation of the effect of microphone cavity geometries on acoustic imaging in wind tunnels, Appl. Acoust. 181 (2021) 108154, http://dx.doi.org/10.1016/j.apacoust.2021.108154.

[8] R. Merino-Martínez, P. Sijtsma, M. Snellen, T. Ahlefeldt, J. Antoni, C.J. Bahr, D. Blacodon, D. Ernst, A. Finez, S. Funke, T.F. Geyer, S. Haxter, G. Herold, X. Huang, W.M. Humphreys, Q. Leclère, A. Malgoezar, U. Michel, T. Padois, A. Pereira, C. Picard, E. Sarradj, H. Siller, D.G. Simons, C. Spehr, A review of acoustic imaging methods using phased microphone arrays (part of the "Aircraft Noise Generation and Assessment" Special Issue), CEAS Aeronaut. J. 10 (1) (2019) 197–230, http://dx.doi.org/10.1007/s13272-019-00383-4.

[9] C.P. VanDercreek, F. Avallone, D. Ragni, M. Snellen, Simulating the acoustic response of cavities to improve microphone array measurements in closed test section wind tunnels, J. Acoust. Soc. Am. 151 (1) (2022) 322, http://dx.doi.org/10.1121/10.0009274.

[10] S. Luesutthiviboon, A.M. Malgoezar, R. Merino-Martinez, M. Snellen, P. Sijtsma, D.G. Simons, Enhanced HR-CLEAN-SC for resolving multiple closely spaced sound sources, Int. J. Aeroacoust. 18 (4–5) (2019) 392–413, http://dx.doi.org/10.1177/1475472X19852938.

[11] S. Guidati, G. Guidati, S. Wagner, Beamforming in a reverberating environment with the use of measured steering vectors, in: 7th AIAA/CEAS Aeroacoustics Conference and Exhibit, Maastricht, The Netherlands, 2001, p. 2166, http://dx.doi.org/10.2514/6.2001-2166.

[12] B.A. Fenech, K. Takeda, Towards more accurate beamforming levels in closed-section wind tunnels via de-reverberation, in: 13th AIAA/CEAS Aeroacoustics Conference (28th AIAA Aeroacoustics Conference), Rome, Italy, 2007, p. 3431, http://dx.doi.org/10.2514/6.2007-3431.

[13] P. Sijtsma, H. Holthusen, Corrections for mirror sources in phased array processing techniques, in: 9th AIAA/CEAS Aeroacoustics Conference and Exhibit, Hilton Head, South Carolina, 2003, p. 3196, http://dx.doi.org/10.2514/6.2003-3196.

[14] J. Fischer, C. Doolan, Beamforming in a reverberant environment using numerical and experimental steering vector formulations, Mech. Syst. Signal Process. 91 (2017) 10–22, http://dx.doi.org/10.1016/j.ymssp.2016.12.025.

[15] S. Gombots, M. Kaltenbacher, B. Kaltenbacher, Combined experimental-simulation based acoustic source localization, in: Proceedings of DAGA, Aachen, Germany, 2016.

[16] M. Lehmann, D. Ernst, M. Schneider, C. Spehr, M. Lummer, Beamforming for measurements under disturbed propagation conditions using numerically calculated Green's functions, J. Sound Vib. 520 (2022) 116638, http://dx.doi.org/10.1016/j.jsv.2021.116638.

[17] R. Merino-Martinez, W. van der Velden, F. Avallone, D. Ragni, Acoustic measurements of a DU96-W-180 airfoil with flow-misaligned serrations at a high Reynolds number in a closed-section wind tunnel, in: 7th International Conference on Wind Turbine Noise, Rotterdam, The Netherlands, 2017.

[18] S. Luesutthiviboon, L.T.L. Pereira, D. Ragni, F. Avallone, M. Snellen, Aeroacoustic benchmarking of trailing-edge noise from NACA 633 –018 airfoil with trailing-edge serrations, AIAA J. 61 (1) (2023) 329–354, http://dx.doi.org/10.2514/1.J061630.

[19] R. Merino-Martínez, P. Sijtsma, A.R. Carpio, R. Zamponi, S. Luesutthiviboon, A.M. Malgoezar, M. Snellen, C. Schram, D.G. Simons, Integration methods for distributed sound sources, Int. J. Aeroacoust. 18 (4–5) (2019) 444–469, http://dx.doi.org/10.1177/1475472X19852945.

[20] COMSOL, Acoustics Module User's Guide, Tech. rep., 1998, URL www.comsol.com/blogs.

[21] Y. Miki, Acoustical properties of porous materials - Modifications of Delany-Bazley models, J. Acoust. Soc. Japan E 11 (1) (1990) 19–24.

[22] D. Oliva, V. Hongisto, Sound absorption of porous materials - Accuracy of prediction methods, Appl. Acoust. 74 (12) (2013) 1473–1479, http://dx.doi.org/10.1016/j.apacoust.2013.06.004.

[23] H. Bento, C.P. Vandercreek, F. Avallone, D. Ragni, P. Sijtsma, M. Snellen, Wall Treatments for Aeroacoustic Measurements in Closed Wind Tunnel Test Sections, AIAA AVIATION Forum, San Diego, CA, 2023, http://dx.doi.org/10.2514/6.2023-4162.

[24] H.F.M. Bento, D. Ragni, F. Avallone, D. Simons, M. Snellen, Acoustic wall treatments for wind tunnel aeroacoustic measurements, Appl. Acoust. 199 (2022) 108989, http://dx.doi.org/10.1016/j.apacoust.2022.108989.

[25] L. Savioja, U.P. Svensson, Overview of geometrical room acoustic modeling techniques, J. Acoust. Soc. Am. 138 (2) (2015) 708–730, http://dx.doi.org/10.1121/1.4926438.

[26] E. Llorente, D. Ragni, Trailing-edge serrations effect on the performance of a wind turbine, Renew. Energy 147 (2020) 437–446, http://dx.doi.org/10.1016/j.renene.2019.08.128.

[27] J. Serpieri, Cross-Flow Instability: Flow Diagnostics and Control of Swept Wing Boundary Layers (Ph.D. thesis), Delft University of Technology, 2018, http://dx.doi.org/10.4233/uuid:3dac1e78-fcc3-437f-9579-048b74439f55.

[28] QSources, QindW miniature sound source, 2024, (Last accessed November 2024). URL https://www.qsources.be/qindw/.

[29] R. Merino-Martínez, A. Rubio Carpio, L.T. Lima Pereira, S. van Herk, F. Avallone, D. Ragni, M. Kotsonis, Aeroacoustic design and characterization of the 3D-printed, open-jet, anechoic wind tunnel of Delft University of Technology, Appl. Acoust. 170 (2020) 107504, http://dx.doi.org/10.1016/j.apacoust.2020.107504.

[30] S. Luesutthiviboon, D. Ragni, Characterization of the acoustically treated low-turbulence tunnel (LTT) of TU Delft, in: Hybrid Anechoic Wind Tunnel (HAWT) Workshop in 26th AIAA/CEAS Aeroacoustics Conference, Online, 2020.

[31] P.D. Welch, The use of fast Fourier transform for the estimation of power spectra: A method based on time averaging over short, modified periodograms, IEEE Trans. Audio Electroacoust. 15 (2) (1967) 70–73, http://dx.doi.org/10.1109/TAU.1967.1161901.

[32] P. Sijtsma, Phased Array Beamforming Applied to Wind Tunnel and Fly-Over Tests, Tech. Rep. NLR-TP-2010-549, National Aerospace Laboratory (NLR), Amsterdam, The Netherlands, 2010, http://dx.doi.org/10.4271/2010-36-0514.

[33] E. Sarradj, Three-dimensional acoustic source mapping with different beamforming steering vector formulations, Adv. Acoust. Vib. 2012 (2012) 292695, http://dx.doi.org/10.1155/2012/292695.